JGR Space Physics

RESEARCH ARTICLE
10.1029/2024JA032521

The Role of the Polar Vortex Jet for Secondary and Higher-Order Gravity Waves in the Northern Mesosphere and Thermosphere During 11–14 January 2016

Sharon L. Vadas[1], Erich Becker[1], Katrina Bossert[2,3], Yuta Hozumi[4,5], Gunter Stober[6], V. Lynn Harvey[7], Gerd Baumgarten[8], and Lars Hoffmann[9]

[1]Northwest Research Associates, Boulder, CO, USA, [2]School of Earth and Space Exploration, Arizona State University, Tempe, AZ, USA, [3]School of Mathematical and Statistical Sciences, Arizona State University, Tempe, AZ, USA, [4]Catholic University of America, Washington, DC, USA, [5]NASA Goddard Space Flight Center, Washington, DC, USA, [6]Oeschger Center for Climate Change Research, Institute of Applied Physics, University at Bern, Bern, Switzerland, [7]Laboratory for Atmospheric and Space Physics, University of Colorado Boulder, Boulder, CO, USA, [8]Leibniz Institute of Atmospheric Physics at the University of Rostock, Kühlungsborn, Germany, [9]Jülich Supercomputing Centre, Forschungszentrum Jülich GmbH, Jülich, Germany

Key Points:

- The vertical shear of the horizontal wind in the entrance, core and exit regions of the polar vortex jet generate GWs in the stratosphere
- Higher-order GWs generated over Europe and Asia propagate over the Arctic then southward over the CONUS at ∼9 − 16 LT due to favorable winds
- Large-scale GWs with $\lambda_H \sim 3{,}000$ km and $c_H \sim 650$ m/s propagate southwestward across the northern thermosphere at ∼8–16 LT

Supporting Information:

Supporting Information may be found in the online version of this article.

Correspondence to:

S. L. Vadas,
vasha@nwra.com

Citation:

Vadas, S. L., Becker, E., Bossert, K., Hozumi, Y., Stober, G., Harvey, V. L., et al. (2024). The role of the polar vortex jet for secondary and higher-order gravity waves in the northern mesosphere and thermosphere during 11–14 January 2016. *Journal of Geophysical Research: Space Physics*, *129*, e2024JA032521. https://doi.org/10.1029/2024JA032521

Received 6 FEB 2024
Accepted 31 JUL 2024

Abstract We analyze the gravity waves (GWs) from the ground to the thermosphere during 11–14 January 2016 using the nudged HI Altitude Mechanistic general Circulation Model. We find that the entrance, core and exit regions of the polar vortex jet are important for generating primary GWs and amplifying GWs from below. These primary GWs dissipate in the upper stratosphere/lower mesosphere and deposit momentum there; the atmosphere responds by generating secondary GWs. This process is repeated, resulting in medium to large-scale higher-order, thermospheric GWs. We find that the amplitudes of the secondary/higher-order GWs from sources below the polar vortex jet are exponentially magnified. The higher-order, thermospheric GWs have concentric ring, arc-like and planar structures, and spread out latitudinally to 10 − 90°N. Those GWs with the largest amplitudes propagate against the background wind. Some of the higher-order GWs generated over Europe propagate over the Arctic region then southward over the US to ∼15–20°N daily at ∼14 − 24 UT (∼9 − 16 LT) due to the favorable background wind. These GWs have horizontal wavelengths $\lambda_H \sim 200 - 2{,}200$ km, horizontal phase speeds $c_H \sim 165 - 260$ m/s, and periods $\tau_r \sim 0.3 - 2.4$ hr. Such GWs could be misidentified as being generated by auroral activity. The large-scale, higher-order GWs are generated in the lower thermosphere and propagate southwestward daily across the northern mid-thermosphere at ∼8–16 LT with $\lambda_H \sim 3{,}000$ km and $c_H \sim 650$ m/s. We compare the simulated GWs with those observed by AIRS, VIIRS/DNB, lidar and meteor radars and find reasonable to good agreement. Thus the polar vortex jet is important for facilitating the global generation of medium to large-scale, higher-order thermospheric GWs via multi-step vertical coupling.

Plain Language Summary Gravity waves (GWs) are perturbations in the Earth's atmosphere created by various processes. When a GW breaks, it imparts momentum to the atmosphere, which in turn can become unbalanced and generate secondary GWs. The same process happens at higher altitudes where the secondary GWs break, thereby generating higher-order GWs. We simulate the primary, secondary and higher-order GWs on 11–14 January 2016 using a GW-resolving whole atmosphere model. We find that the entrance, core and exit regions of the jet that encircles the polar vortex generate primary GWs. In addition, the polar vortex jet magnifies the amplitudes of higher-order GWs from sources below the jet, such as mountain waves. The resulting higher-order GWs have horizontal wavelengths of hundreds to thousands of km with concentric ring, arc-like and planar structures in the thermosphere. We compare the simulated GWs with AIRS, VIIRS/DNB, lidar, and meteor radar observations and find reasonable to good agreement.

1. Introduction

Primary atmospheric GWs are generated by a variety of processes, including deep convection (Fovell et al., 1992; Heale et al., 2019; Holton & Alexander, 1999; Holt et al., 2017; Horinouchi et al., 2002; Lane et al., 2001; Stephan & Alexander, 2015; Taylor & Hapgood, 1988; Vadas et al., 2009; Walterscheid et al., 2001; Yue et al., 2009), wind flow over topography (Alexander & Teitelbaum, 2011; Becker & Vadas, 2018; Eckermann & Preusse, 1999; Fritts et al., 2016, 2021; Hindley et al., 2021; Hoffmann et al., 2013; Jiang et al., 2004; Lund

et al., 2020; Plougonven et al., 2008; Sato et al., 2012; Vadas & Becker, 2019; Walterscheid et al., 2016; Watanabe et al., 2006), tropospheric jets and fronts (O'Sullivan & Dunkerton, 1995; Plougonven & Zhang, 2014; Vadas & Fritts, 2001; Zhang, 2004; Zülicke & Peters, 2006), and spontaneous emission from the stratospheric polar vortex (Becker, Vadas, et al., 2022; Chen et al., 2013; Sato & Yoshiki, 2008; Shibuya et al., 2017; Vadas, Becker, Bossert, et al., 2023; Yoshiki & Sato, 2000; Yoshiki et al., 2004). Most of these primary GWs break in the stratosphere and mesosphere due to dynamic instability induced by the background winds and the approximate exponential growth with height z of the GW amplitudes (e.g., Fritts & Alexander, 2003).

In addition to generating GWs, the polar vortex jet can also amplify westward-propagating GWs from below via kinetic energy transfer from the mean flow to the GWs in regions of eastward vertical wind shear (Becker, Vadas, et al., 2022). Slow intrinsic westward-propagating GWs such as mountain waves (MWs) have increased vertical wavelengths λ_z when they propagate through the polar vortex jet, since $|\lambda_z|$ is proportional to the background wind for these GWs. The increased $|\lambda_z|$ increases their stability and delays their breaking until they reach $z \sim 50 - 70$ km, which is at or above the polar vortex jet maximum (e.g., Vadas & Becker, 2019; Vadas, Becker, Bossert, et al., 2023).

Upon breaking, small-scale secondary GWs are generated from nonlinear processes (e.g., Achatz, 2007; Chun & Kim, 2008; Fritts et al., 2013; Heale et al., 2022; Li et al., 2005; Lund & Fritts, 2012; Mixa et al., 2021; Snively & Pasko, 2003). The accompanying momentum and energy deposition changes the wind and temperature structure of the atmosphere (Holton, 1983). Because the small-scale, nonlinearly generated secondary GWs typically have small horizontal phase speeds (<50 m/s), they often do not propagate very far before being reabsorbed by the atmosphere (often within the horizontal extent of the breaking wave packet), and therefore can be loosely thought of as being part of the transition to smaller horizontal and vertical scales and the cascade to turbulence. However, they can transport significant momentum flux (e.g., Bossert et al., 2017; Fritts et al., 2002), and therefore can contribute significantly to the deposition of momentum and energy where they are reabsorbed. In this paper, we define small, medium and large scales as $\lambda_H < 100$ km, $100 \leq \lambda_H < 1{,}000$ km, and $1{,}000 \leq \lambda_H < 5{,}000$ km, respectively.

Since the momentum and energy deposition that result from wave breaking is highly variable temporally and spatially, the atmosphere becomes unbalanced and generates a different type of secondary GWs (Vadas et al., 2003, 2018). These latter secondary GWs are upward and downward-propagating, have concentric ring structure, and have horizontal wavelengths ranging from a fraction of the primary GW horizontal wavelength to several times the horizontal extent of the primary GW packet (e.g., Heale et al., 2022; Vadas & Becker, 2019; Vadas & Liu, 2009, 2013), depending on whether or not there is constructive/destructive interference among wave packets from different sources (Vadas & Becker, 2018; Vadas & Crowley, 2010). These latter secondary GWs can propagate large distances (e.g., Vadas & Becker, 2019; Vadas & Liu, 2013), as was recently demonstrated and verified observationally after the Hunga Tonga-Hunga Ha'apai volcanic eruption on 15 January 2022 (Vadas, Becker, Figueiredo, et al., 2023; Vadas, Figueiredo, et al., 2023). This process repeats itself; the secondary GWs break/dissipate and deposit their momentum and energy, whereby the atmosphere responds to being unbalanced by generating higher-order GWs (Vadas & Becker, 2019).

The process discussed above by which the atmosphere generates secondary and higher-order GWs is called "multi-step vertical coupling" (MSVC). At each step in this process, GW breaking/dissipation results in momentum and energy deposition, which unbalances the atmosphere; the atmosphere responds by generating upward and downward-propagating higher-order GWs with concentric ring structure and with initially smaller amplitudes than the primary GWs. The horizontal and vertical wavelengths of the higher-order GWs depend sensitively on the sources and complexity of the GW field, ranging from small scales (Kogure et al., 2020) to medium scales (Vadas & Azeem, 2021; Vadas & Becker, 2019), to large scales (Vadas & Liu, 2009, 2013; Vadas, Becker, Figueiredo, et al., 2023). In this paper, we use the terms secondary and higher-order GWs interchangeably to refer only to those GWs generated by the atmosphere's response to momentum and energy deposition from GW breaking and/or from dissipation by molecular viscosity or ion drag in the thermosphere. It is important to note that current GW parameterization schemes do not account for higher-order GWs.

A recent paper examined the upward and downward-propagating GWs within two "fishbone" structures observed at $z = 45 - 75$ km on 12–14 January 2016 by the Rayleigh lidar at the Arctic Lidar Observatory for Middle Atmosphere Research (ALOMAR) in Norway at 16.08°E, 69.38°N (Vadas, Becker, Bossert, et al., 2023) (hereafter V23). (Here, a fishbone structure in an altitude-time plot contains upward-propagating GWs above a central "knee" altitude, and downward-propagating GWs below this knee altitude. Note that the downward and

upward phase lines converge at the knee altitude, which is the altitude of the horizontally displaced local body force (LBF)). Those GWs were propagating northwest and northward away from the polar vortex jet, and had medium to large scales. That work simulated this event with the nudged HIAMCM, which simulates GWs explicitly (Becker & Vadas, 2020; Becker, Goncharenko, et al., 2022; Becker, Vadas, et al., 2022). V23 found that primary GWs were generated by the core of the polar vortex jet over Europe at 52–54°N at $z \sim 25 - 40$ km and dissipated at ∼35°E, ∼60°N and $z \sim 54 - 60$ km. Here we define the "core" of the polar vortex jet as being the region(s) where the wind is maximum in the stratospheric jet. (In this case, the wind in the polar vortex jet core was maximum at $z \sim 50$ km.) The resulting LBFs generated upward and downward-propagating secondary GWs that propagated horizontally and were subsequently observed by the ALOMAR lidar. Excellent agreement was found between the simulated GWs and observations made by the Rayleigh lidar at ALOMAR and by the Atmospheric InfraRed Sounder (AIRS). That work noted that the amplitudes of some of the secondary GWs ceased growing exponentially at/above $z \sim 75$ km (in both the model and observations) (Figures 8a and 8b of V23), thereby suggesting that these secondary GWs were dissipating at/above $z \sim 75$ km. If so, higher-order GWs would have been generated at these altitudes.

The purpose of this paper is to determine the role that the entrance, core and exit regions of the polar vortex jet have in generating/amplifying primary GWs which, through multiple dissipation/excitation cycles, generate higher-order GWs that then propagate in the winter thermosphere during 11–14 January 2016. Here we define the "entrance" region where the wind is constricted into a smaller area of the jet core with increasing wind speed, and the exit region where the air is expanding out of the core into a larger area with decreasing wind speed. During this time, a global reanalysis study showed that the polar vortex was the strongest and coldest as during the previous 68 years (Matthias et al., 2016), which led to an unusual circulation in the mesosphere during January 2016 (Stober et al., 2017). These conditions were accompanied by large amplitudes of the stationary planetary wave in the subtropical mesosphere (Matthias & Ern, 2018).

In this paper we simulate 11–14 January 2016 using the nudged HIAMCM. This model successfully simulated the secondary GWs generated by the polar vortex jet (V23) and from the Hunga Tonga-Hunga Ha'apai volcanic eruption (Vadas, Becker, Figueiredo, et al., 2023; Vadas, Figueiredo, et al., 2023). Because the model does not include geomagnetic forcing, all simulated GWs are generated from neutral atmospheric processes. We review the nudged HIAMCM in Section 2. In Section 3, we compare the simulated results with lidar data at ALOMAR, and we investigate the primary and higher-order GWs generated/amplified by the entrance, core and exit regions of the polar vortex jet from the ground to the thermosphere. Section 4 presents a comparison of the simulated GWs with AIRS, VIIRS/DNB and meteor radar observations. Section 5 contains our conclusions and a discussion. Appendix A shows a comparison of the HIAMCM temperatures with those measured by ACE-FTS and SOFIE.

2. The HIAMCM

The HIAMCM is a high-resolution, whole-atmosphere model for the neutral dynamics (Becker & Vadas, 2020). It employs a spectral dynamical core with a terrain-following hybrid vertical coordinate, a correction for non-hydrostatic dynamics, and consistent thermodynamics in the thermosphere. This model utilizes a triangular spectral truncation at wavenumber 256, corresponding to a horizontal grid spacing of ∼52 km. The current version has an altitude-dependent vertical resolution up to $z \sim 450$ km, includes 280 levels, and has an effective horizontal resolution of $\lambda_H \simeq 200$ km. Resolved GWs are dissipated predominantly by macro-turbulent diffusion at $z < 200$ km using a classical Smagorinsky-type diffusion scheme (Becker & Vadas, 2020), and by molecular diffusion at higher altitudes. Topography and a simple ocean model are fully taken into account, as well as radiative transfer, boundary layer processes, and the tropospheric moisture cycle. The initial condition for this HIAMCM run is from the free-running HIAMCM in late December (Becker & Vadas, 2020). In order to simulate observed events, the large scales of the HIAMCM ($\lambda_H > 2{,}000 - 2{,}500$ km) are then nudged from the ground to $z \sim 70$ km to NASA's Modern-Era Retrospective analysis for Research and Applications, Version 2 (MERRA-2) reanalysis data (Gelaro et al., 2017). An adjustment period of 7–10 model days is necessary after the nudging is turned on before using/analyzing the nudged HIAMCM data. The model data we use here is identical to that used in V23, except that a simple ion drag parameterization has been added (described in Becker, Goncharenko, et al. (2022)) that drives the auroral circulation from the dayside to the nightside over the poles in the thermosphere (Forbes, 2007). Further details of the HIAMCM are given in Becker, Vadas, et al. (2022) and references therein.

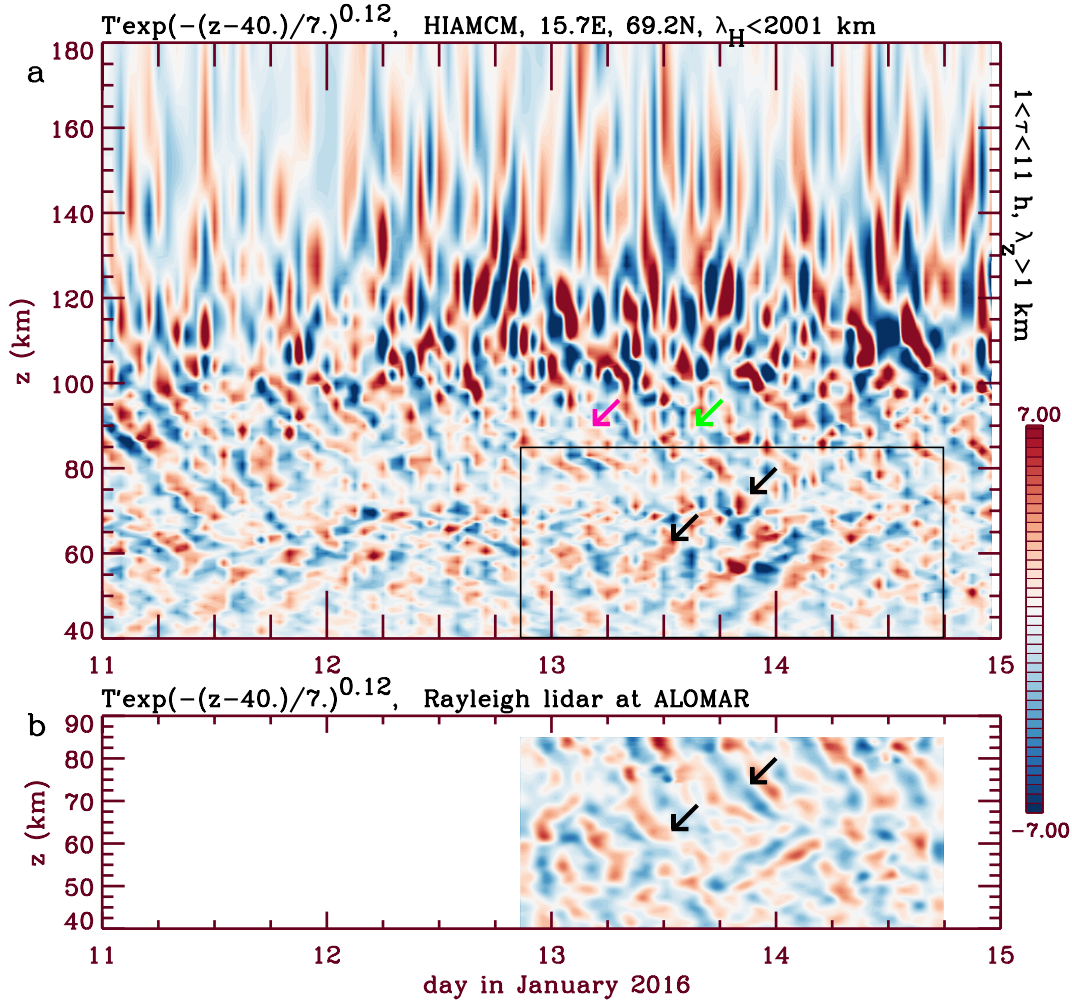

Figure 1. Keogram of the scaled temperature perturbations, $T'[\exp(-(z-40)/7)]^{0.12}$ (colors, in K) on 11–14 January 2016, where z is in km. (a) HIAMCM results at 15.7°E, 69.2°N for perturbations with $\lambda_H < 2{,}001$ km. (b) Raleigh lidar observations at ALOMAR. All perturbations contain GWs with $1 < \tau_r < 11$ hr and $|\lambda_z| \geq 1$ km. The colors are oversaturated to see the GWs. The black rectangle in (a) shows the period containing the lidar data. The black arrows indicate the secondary GWs in events #1 and #2 analyzed in V23. The pink and green arrows in (a) indicate where the secondary GWs in events #1 and #2, respectively, dissipate.

3. Primary and Higher-Order GWs From the Polar Vortex Jet

3.1. Comparison of Simulated and Observed GWs at ALOMAR

Figure 1a shows a keogram of the "exponentially scaled" temperature perturbations,

$$T' \, e^{\{-(z-40\text{km})/\mathcal{H}\}^{0.12}}, \tag{1}$$

in the HIAMCM on 11–14 January at ALOMAR for GWs with $\lambda_H \leq 2{,}001$ km (global wavenumbers ≥20). Here, T is temperature, primes denote perturbations, z is in km and $\mathcal{H} = 7$ km. We choose the power of the exponential, $p = 0.12$, subjectively to visualize both the primary and higher-order GWs with the same color scale. If a primary GW propagates from $z = 0$ to 180 km with no dissipation, then because $T' \propto \overline{\rho}^{\,-1/2} \propto \exp(z/\mathcal{H})^{0.5}$ (Hines, 1960), we would choose $p = 0.5$. However, because both the primary and secondary GWs dissipate (see below), we must choose $0 < p < 0.5$ in order to see the GWs from the stratosphere to the thermosphere. Note that our choice of p does not create an artificial "zero" in the scaled temperature perturbations in Figure 1 because $e^{\{-(z-40\text{km})/\mathcal{H}\}^{0.12}}$ is a monotonically decreasing function.

In the stratosphere, mesosphere and lower thermosphere, a "checkerboard" appearance is seen in T' caused by the constructive/destructive interference of upward and downward-propagating GWs. The phase lines of the largest-amplitude GWs mainly go upward in time at $z = 40$–60 km, and mainly go downward in time at $z = 60$–100 km. When the phase lines of GWs go upward and downward in time, the GWs propagate downward and upward in time, respectively, if the background wind along the GW propagation direction, U_H, is smaller than the GW horizontal intrinsic phase speed c_{IH} (e.g., Fritts & Alexander, 2003), (see also the text surrounding Equation 60 in Vadas et al., 2018). We showed that this condition is met for these GWs in V23; thus the largest-amplitude GWs in Figure 1a mainly propagate downward at $z = 40$–60 km, and mainly propagate upward at $z = 60$–110 km. These GWs are the secondary GWs generated at $z \sim 60$ km.

The simulated GWs in the stratosphere and mesosphere have $T' \sim 5 - 20$ K, periods of $\tau_r \sim 4 - 10$ hr and vertical wavelengths of $|\lambda_z| \sim 10 - 20$ km. The black arrows indicate some of the lower-frequency GWs in events #1 and #2 that were previously identified as secondary GWs from the polar vortex jet which propagated to ALOMAR (V23). Note that the secondary GWs generated by a single LBF contain a broad spectrum of slow to fast upward and downward-propagating GWs with a broad range of horizontal and vertical wavelengths. At a given time and horizontal distance from a LBL, those secondary GWs with larger intrinsic frequencies ω_{Ir} and faster vertical group velocities (having larger ascent angles from the horizontal and larger $|\lambda_z|$) reach higher altitudes than those secondary GWs with smaller ω_{Ir} and slower vertical group velocities (having smaller ascent angles and smaller $|\lambda_z|$). This results in the characteristic "fishbone" structure seen in Figure 1a (V23). The source location of the secondary GWs in event #1 was found to be ∼1,400 km southeast of ALOMAR at ∼35°E, ∼60°N and $z \sim 54 - 60$ km in that work. Figure 1b shows the corresponding keogram from the available Rayleigh lidar observations at ALOMAR. Upward and downward-propagating GWs with T', τ_r, and $|\lambda_z|$ similar to Figure 1a are seen, thereby providing good validation of the secondary GWs simulated by the model. Typical secondary GW amplitudes are $T' \sim 6 \times \exp((70 - 40)/7)^{0.12} \simeq 10$ K at $z = 70$ km (where we have substituted $z = 70$ km into Equation 1) and $T' \sim 10 \times \exp((100 - 40)/7)^{0.12} \simeq 30$ K at $z = 100$ km. Note that the *primary* GWs from the polar vortex jet simulated by the model were validated with AIRS data (see Figure 9 of V23). The amplitudes of the higher-frequency secondary GWs in events #1 and 2 in Figure 1a become quite small at $z \sim 90 - 100$ km because the GWs dissipate there; these GWs are indicated by pink and green arrows, respectively.

At $z > 100 - 110$ km, the phase lines are much steeper in Figure 1a due to the GWs having larger $|\lambda_z|$ and smaller τ_r. For example, the GWs at $z = 180$ km have $\lambda_z \sim 100 - 200$ km and $\tau_r \sim 1 - 4$ hr, with $T' \simeq (3$–$5) \times \exp((180 - 40)/7)^{0.12}$ K $\simeq (30 - 55)$ K. Because a GW's τ_r does not change in altitude unless the background wind varies rapidly in *time* (Lighthill, 1978; Senf & Achatz, 2011), the dramatic decrease in τ_r from $z \sim 90$ to $z \sim 110$ km shows that the GWs at $z \sim 110$ km are different than those at $z = 90$ km. The dramatic decrease in τ_r over such a short vertical distance raises the possibility that the thermospheric GWs may be higher-order GWs, rather than fast secondary GWs that propagate through the strong wind in the MLT without breaking.

Figure 2 shows the corresponding keograms for the scaled horizontal wind perturbations,

$$u' \, e^{\{-(z-40\text{km})/\mathcal{H}\}^{0.12}}, \qquad v' \, e^{\{-(z-40\text{km})/\mathcal{H}\}^{0.12}}, \tag{2}$$

where u' and v' are the zonal and meridional velocity perturbations (of the air/fluid). Upward and downward-propagating GWs with τ_r and λ_z similar to Figure 1 are seen. Good agreement is seen between the simulated and observed GWs during the overlap periods, especially at $z \sim 40 - 70$ km. Notable differences occur above 70 km, which may be due to the fact that the large-scale wind in the HIAMCM is only weakly nudged above 40 km and is not nudged above 70 km, thereby causing the large-scale winds, and hence the simulated GWs, to differ from the real atmosphere at $z > 70$ km. At $z = 180$ km, u', $v' \simeq (2$–$4) \times \exp((180 - 40)/7)^{0.12}$ m/s $\simeq (20 - 45)$ m/s (where we have substituted $z = 180$ km into Equation 2). We note that GWs with upward phase lines in time often occur at 110 km $< z <$ 140 km and sometimes occur at 140 km $< z <$ 180 km (e.g., at 12.6 − 13 January at $z \sim 120 - 180$ km) in Figures 1 and 2. Some of these GWs may be downward-propagating GWs that are generated by LBFs created by the dissipation of upward-propagating higher-order GWs in the thermosphere.

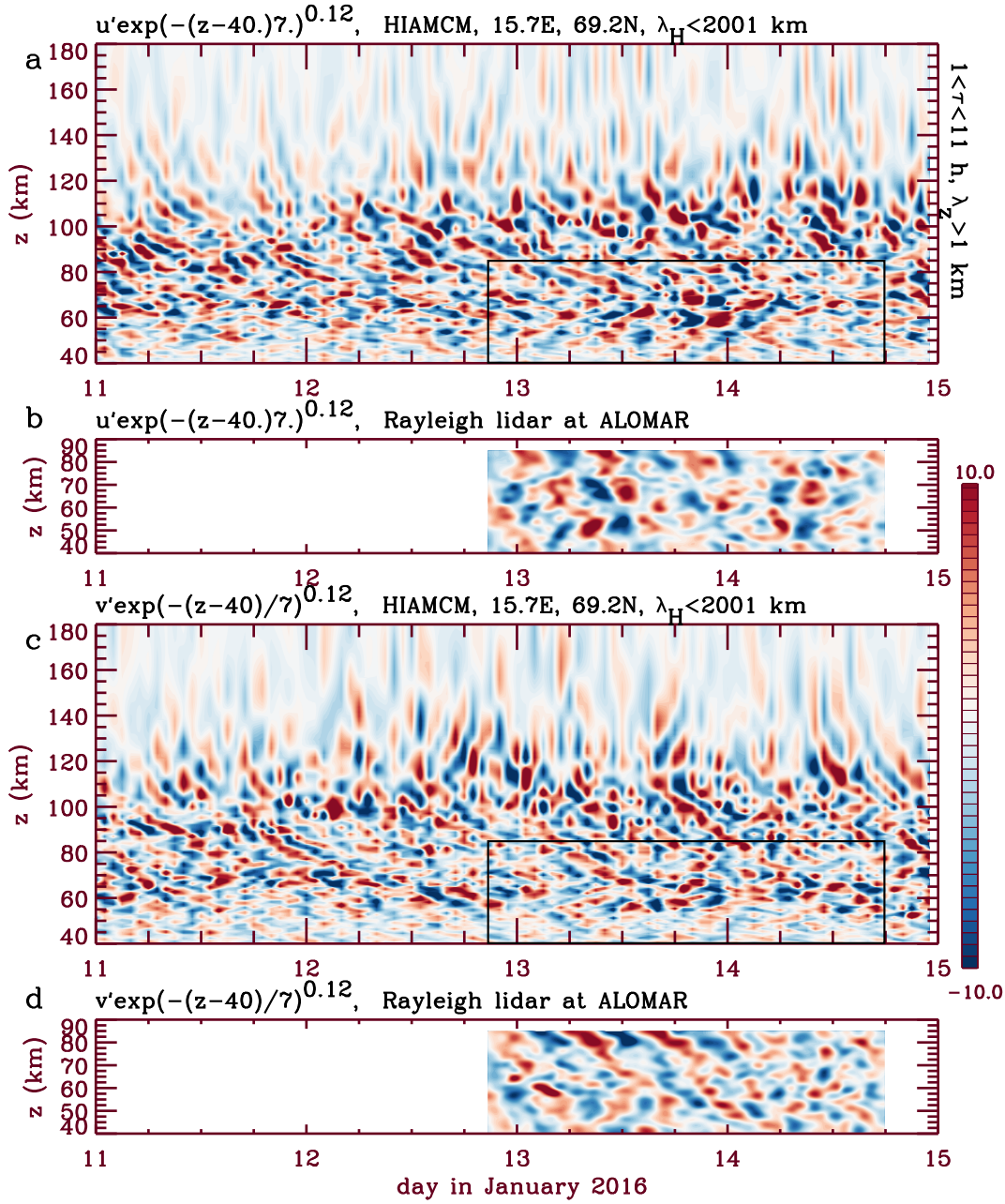

Figure 2. (a and b) Keogram of $u'[\exp(-(z-40)/7)]^{0.12}$ (colors, in m/s) on 11–14 January 2016, where z is in km. (a) HIAMCM results at 15.7°E, 69.2°N for GWs with $\lambda_H < 2{,}001$ km. (b) Raleigh lidar observations at ALOMAR. (c and d) Same as (a and b) but for $v'[\exp(-(z-40)/7)]^{0.12}$. All perturbations contain GWs with $1 < \tau_r < 11$ hr and $|\lambda_z| \geq 1$ km. The colors are oversaturated to see the GWs. The black rectangles in (a, c) show the period containing the lidar data.

3.2. Primary and Higher-Order Medium to Large-Scale GWs

3.2.1. Role of the Wind Shear, and Latitudinal Spreading of Higher-Order GWs

Figure 3a shows $T'\left(\overline{\rho}/\rho_0\right)^{0.12}$ as a function of latitude and z at 15.7°E (the longitude of ALOMAR) from the HIAMCM at 12 UT on 13 January during event #1. MWs generated by orographic forcing over the Alps occur at 40 − 50°N (gray arrow), and primary "X-structure" GWs generated in the shear in the core of the polar vortex jet occur at 48 − 55°N (black arrow), as was shown in V23. (Here, an X-structure shows upward-northward and upward-southward propagating GWs above the generation altitude and downward-northward and downward-

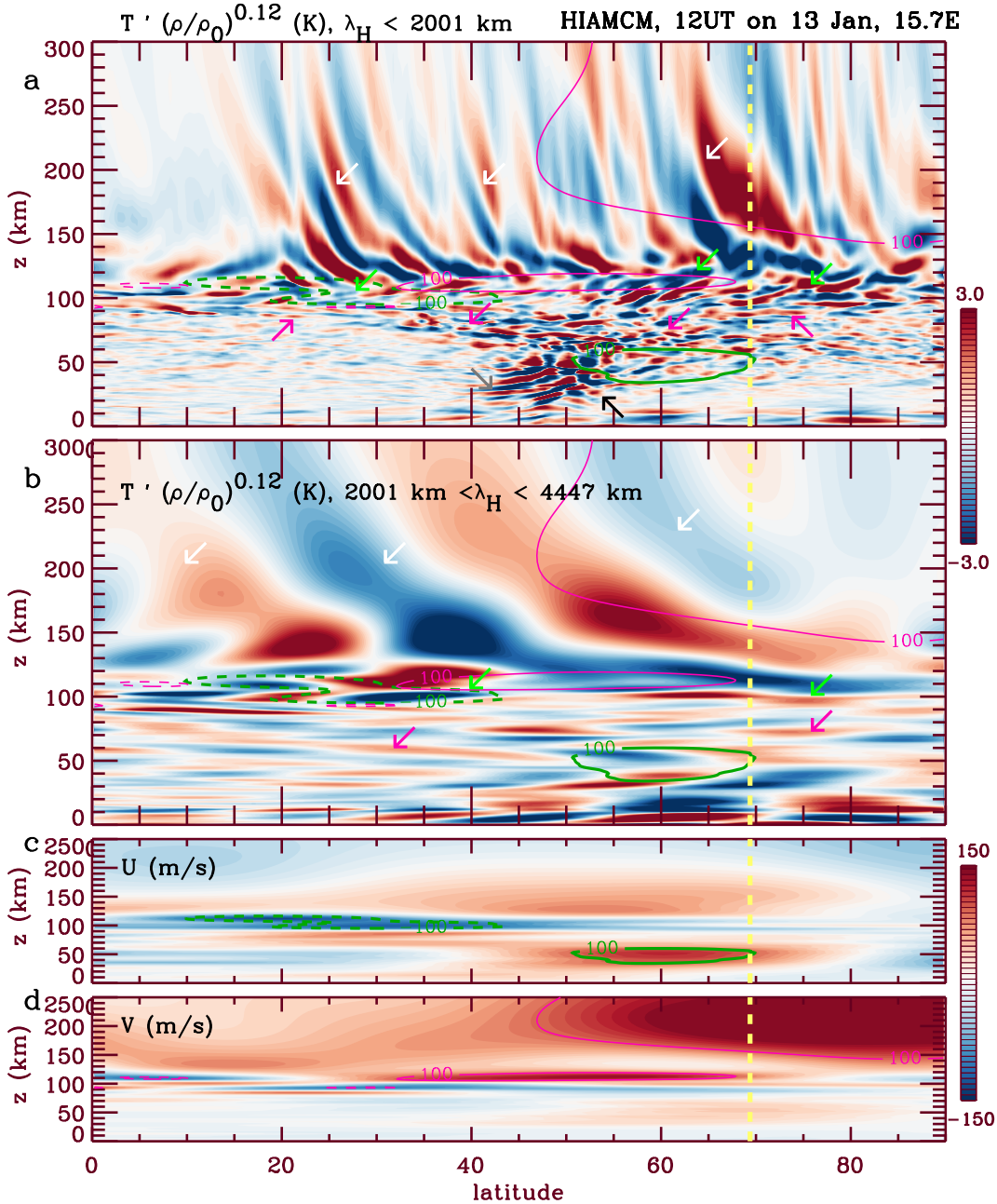

Figure 3. HIAMCM results as a function of latitude and z at 15.7°E at 12 UT on 13 January 2016. (a) $T'\left(\overline{\rho}/\rho_0\right)^{0.12}$ (color, in K) for GWs with $\lambda_H < 2{,}001$ km, where $\rho_0 = 1{,}247$ g/m^3. Gray and black arrows indicate mountain waves and GWs from the polar vortex jet, respectively. The arrows indicate secondary GWs (pink), higher-order GW generation regions (green), and higher-order GWs (white). (b) Same as (a) but for GWs with $2{,}001 < \lambda_H < 4{,}447$ km. (c and d) $\overline{U}$ and $\overline{V}$, respectively, (color, in m/s) which are the background zonal and meridional wind from the HIAMCM for waves with $\lambda_H > 4{,}447$ km. The z range (c and d) is different from (a and b). Green and pink lines show ±100 m/s contours for $\overline{U}$ and $\overline{V}$, respectively, with solid (dash) lines denoting positive (negative) values. ALOMAR's location is shown with the yellow dash line.

southward propagating GWs below the generation altitude in a latitude-altitude plot, as was discussed in V23.) That work showed that X-structure GWs are generated by the zonal wind shear at the equatorward edge of the polar vortex jet beneath the altitude where the jet speed is maximum. This location is confirmed by the green contour showing $\overline{U} = 100$ m/s in Figure 3a (see also Figure 3c). In this paper, we define the background zonal and meridional wind, $\overline{U}$ and $\overline{V}$, as containing all waves from the HIAMCM with total horizontal wavenumber <9

(with respect to spherical harmonics decomposition), which corresponds to $\lambda_H > 4{,}447$ km. As shown in V23, the primary GWs from the polar vortex jet propagate upward and downward, and north/northwestward and south/southeastward, then dissipate at $z \sim 55-65$ km. The atmosphere responds by generating secondary GWs that propagate poleward and equatorward away from their source (pink arrows in Figure 3a).

As discussed above, the secondary GWs over ALOMAR have large wave periods of $\tau_r \sim 4-10$ hr (see Figures 1 and 2). They also have large intrinsic periods of $\tau_{Ir} \sim 3-7$ hr (Figure 6b of V23). The ascent angle of a GW from the horizontal, ζ, is determined via $\sin\zeta \simeq \tau_B/\tau_{Ir}$, where τ_B is the buoyancy period (e.g., Equation 19 of Vadas et al., 2009). Since $\tau_{Ir} \gg \tau_B$, the ascent angle from the horizontal is small for most of the secondary GWs over ALOMAR. Such small ascent angles can be seen in Figure 3a at $z \sim 70-100$ km. This causes the secondary GWs to cover large distances horizontally as they propagate vertically to the MLT (pink arrows). This results in the secondary GWs covering the large latitude range of $\sim 20-90°$ N when they reach the MLT. Upon reaching the strong zonal and meridional background winds in the MLT (with amplitudes in excess of 100 m/s), the secondary GWs dissipate, as indicated by the rapidly decreasing/vanishing amplitudes there. Upon dissipating and depositing momentum/energy locally, the atmosphere is unbalanced and responds by generating upward and downward-propagating higher-order GWs, as shown theoretically (Vadas et al., 2003, 2018). Several regions where upward and downward-propagating GWs with much larger meridional and vertical wavelengths (than the GWs propagating upward from below) are generated in the MLT are indicated with green arrows in Figure 3a. These regions are associated with strong wind shears. For example, higher-order GWs are generated at $z \sim 100-120$ km above (a) a strong meridional wind shear of $\sim$10 m/s/km with $\max(\overline{V}) \sim 100$ m/s at $30-70°$N, and (b) a strong zonal wind shear of $\sim$10 m/s/km with $\max(\overline{U}) \sim -100$ m/s at $10-40°$N.

The upward-propagating higher-order GWs propagate well into the thermosphere (white arrows in Figure 3a), and mainly travel southward at this time due to the northward background wind (see Figures 3c and 3d). Some GWs propagate to $z \sim 300$ km while others dissipate at $z \sim 200$ km; this variability in dissipation altitude occurs because the GW spectrum from a LBF contains a large range of horizontal and vertical wavelengths (Vadas et al., 2018), and a GW's dissipation altitude depends sensitively on λ_z (Vadas, 2007).

Finally, note that the MWs over the Alps in Figure 3a are south of the polar vortex jet edge and appear to dissipate at $z \sim 30-40$ km where the background wind is weakly eastward (Figure 3c). This dissipation altitude, $z \sim 30-40$ km, was estimated in V23 using mesoscale kinetic energy source (MKS) theory. That work also showed that the morphology of the MKS signatures for MWs and GWs from the polar vortex jet are distinct, with a separation between the two sources roughly occurring south and north of 50°N, respectively. Although the dissipation of MWs in Figure 3a also generates secondary GWs, these secondary GWs likely have smaller amplitudes in the mesosphere and lower thermosphere (MLT) as compared to the secondary GWs generated by the primary GWs from the polar vortex jet because of the "magnifying glass" effect of the polar vortex jet combined with MSVC (see Section 3.2.3 for a detailed description of this effect). However MWs may play a significant or even dominant role during other periods or in other locations (e.g., over the winter Southern Andes, see Vadas and Becker (2019)).

Movie S1 shows a latitude-altitude slice of $T' e^{\{-(z-40\text{km})/\mathcal{H}\}^{0.12}}$ at 15.7°E from the HIAMCM at 11–14 January 2016 using $\mathcal{H} = 7$ km. GWs are generated by the polar vortex jet at $z \sim 30-60$ km and $\sim 50-70°$N throughout this period (green contours show $\overline{U} = 100$ m/s). MWs over the Alps are also occasionally seen. Movie S2 shows the same slice but at 20°W (over the Atlantic Ocean). X-structure GWs are generated by the polar vortex jet at $z \sim 30-40$ km and $\sim$50°N. Secondary and higher-order GWs are seen in the mesosphere and thermosphere.

Figure 3b shows the higher-order GWs with $2{,}001 < \lambda_H < 4{,}447$ km from the polar vortex jet. Large-scale upward and downward-propagating GWs are generated at $z \sim 100-110$ km. These GWs propagate southward. Those that propagate upward reach $z \sim 200-300$ km (white arrows), while those that propagate downward vanish at $z \sim 90$ km. Note that the amplitudes of the upward-propagating GWs decrease significantly above $z \sim 160-200$ km, indicating that these GWs likely dissipate from molecular viscosity and ion drag.

Figures 4a–4c shows latitude-altitude slices of T', u', and v' from the HIAMCM at 15.7°E and $z = 50-110$ km at 12 UT on 13 January 2016 for GWs with $\lambda_H < 2{,}001$ km. Row 2 shows the corresponding longitude-altitude slices at 39.7°N. Typical GWs have $T' \sim 10-50$ K, $u', v \sim 20-60$ m/s, and $\lambda_H \sim 150-400$ km, the latter of which extends to the resolution scale of the HIAMCM. Since these GWs have $|\lambda_z| > 8$ km and $T' > 5-10$ K, they could

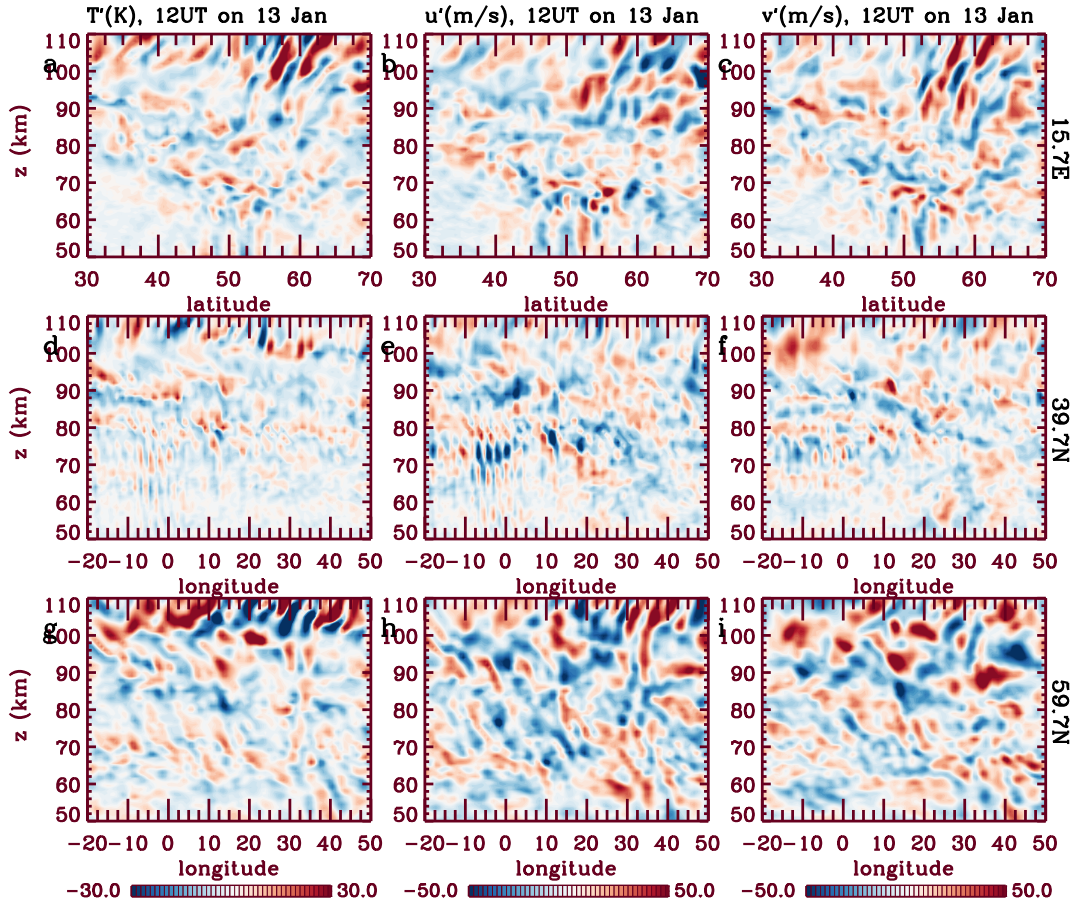

Figure 4. HIAMCM T' (in K, column 1), u' (in m/s, column 2) and v' (in m/s, column 3) at 12 UT on 13 January 2016 for GWs with $\lambda_H < 2{,}001$ km. Row 1: Latitude-altitude slice at 15.7°E. Row 2: Longitude-altitude slice at 39.7°N. Row 3: Longitude-altitude slice at 59.7°N.

observed by OH airglow (e.g., Taylor & Hapgood, 1988). Row 3 shows the corresponding GWs at 59.7°N. These GWs have somewhat larger λ_H and larger amplitudes.

3.2.2. GWs From the Entrance, Core, and Exit Regions of the Polar Vortex Jet

Figure 5 shows T' on 13 January from the HIAMCM at 0 and 12 UT at z = 40 and 70 km for GWs with $\lambda_H < 2{,}001$ km. Vectors show $(\overline{U},\overline{V})$. The background wind speed at $z = 50$ km, $\sqrt{\overline{U}^2 + \overline{V}^2}$, corresponding to the stratospheric polar vortex jet, is shown as green contours in Figure 5a. The polar vortex jet is characterized by two main jet cores (Figure 12 of Bossert et al., 2020). The larger jet core extends over the United Kingdom/northern Europe ("major" core) and the smaller core extends over the Arctic Ocean north of Alaska ("minor" core). The maximum wind speed of the major core is ∼160 m/s (Figure 4 of V23).

The largest-amplitude GWs have $T' \sim 20 - 35$ K and are seen at $z = 40$ km over northern Europe, with phase lines *parallel* to the background flow (green arrows in Figures 5a and 5b). These GWs are generated/amplified in the *major core* of the polar vortex jet, as was shown previously (V23). (Here, the polar vortex jet "amplifies" the amplitude of an existing GW that propagates from below, such as a MW.) GWs with $T' \sim 3$ K are also seen over the Arctic Ocean north of the Asian continent and Alaska having phase lines approximately parallel to the background flow (green arrows). These latter GWs are significantly weaker than those over northern Europe, and are generated/amplified in the *minor core* of the polar vortex jet. In addition, GWs are seen at $z = 40$ km having phase lines approximately perpendicular to the background flow (a) over the *exit region of the major core* of the polar vortex jet over the Asian continent at 80–120°E and 40–70°N with $T' \sim 5$ K (purple arrows) and (b) over the *entrance region of the minor core* of the polar vortex jet over the Asian continent at 120–150°E and 40–80°N in

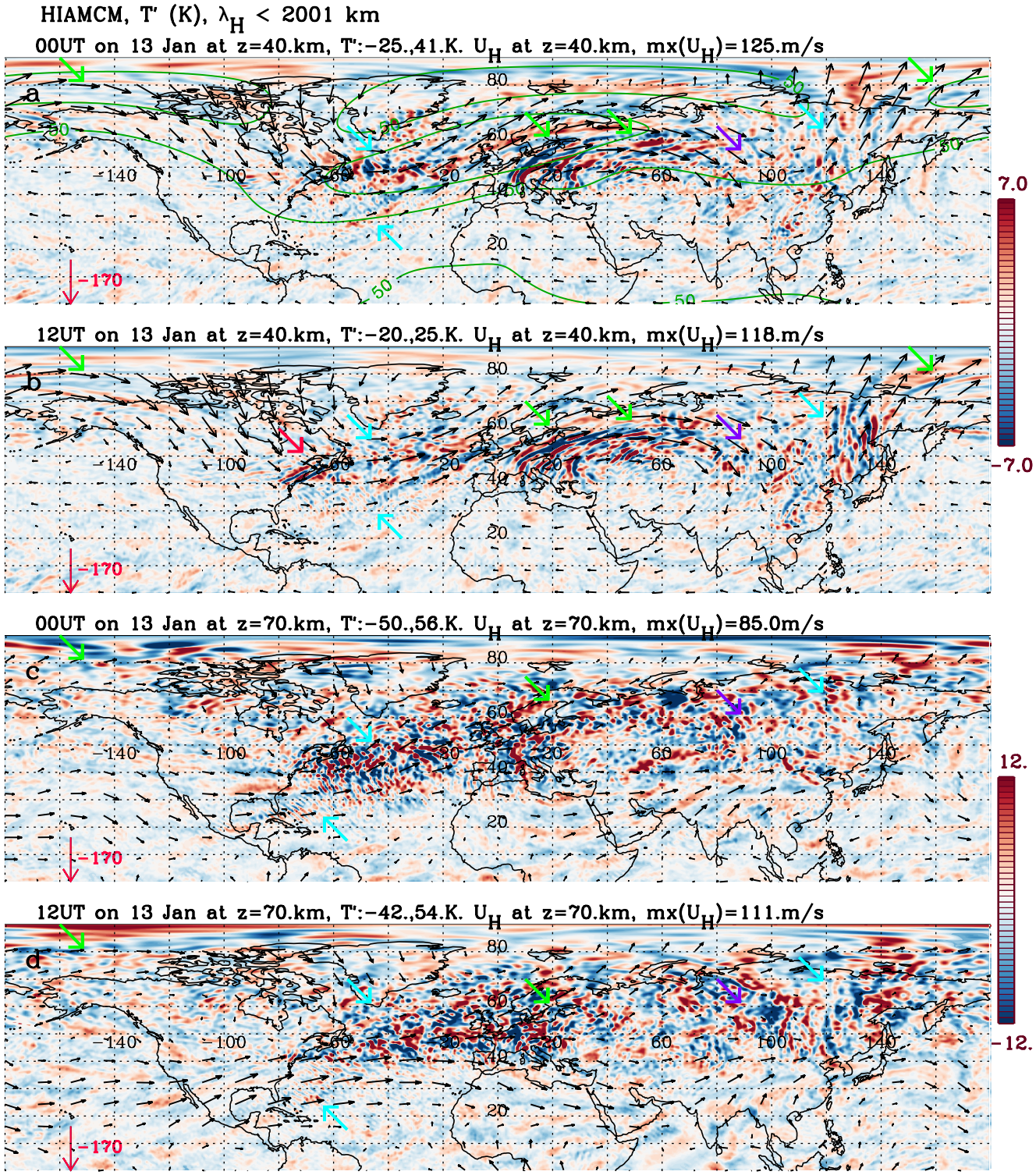

Figure 5. T' (colors, in K) at 0 UT (a) and 12 UT (b) on 13 January 2016 from the HIAMCM at $z = 40$ km for GWs with $\lambda_H < 2{,}001$ km. Rows 3 and 4: Same as rows 1 and 2 except at $z = 70$ km. Vectors show $(\overline{U}, \overline{V})$ at each altitude. The downward red arrows in the lower left-hand corners show $\overline{V} = -170$ m/s. Green contours in (a) show $\overline{U}_H = \sqrt{\overline{U}^2 + \overline{V}^2} = 50$, 100 and 150 m/s at $z = 50$ km. Arrows show primary and higher-order GWs from the entrance (turquoise), core (green) and exit (purple) regions of the polar vortex jet. The red arrow in (b) shows MWs over the Appalachian Mountains. Minimum and maximum values of T' and $\overline{U}_H$ are given in each caption. The colors are oversaturated to see the GWs.

Figures 5a and 5b with $T' \sim 5-15$ K (turquoise arrows). Here, the entrance region occurs where the air constricts into a smaller area of the jet core with increasing wind speed and the exit region occurs where the air expands out of the core into a larger area with decreasing wind speed (see green contours in Figure 5a). The entrance and exit regions are characterized by significant vertical wind shear (see Section 3.4). The constructive/destructive interference patterns of T' in the exit region are caused by the interference of multiple GW packets from different parts of the exit/entrance regions. Note that the morphology of the entrance region GWs over Asia in Figure 5b (turquoise arrow) looks similar to the GWs generated in the tropospheric jet exit regions (e.g., O'Sullivan & Dunkerton, 1995). Note that the GWs in Figures 5a and 5b may be upward or downward-propagating.

In addition, MW events occur over the Alps and Carpathian Mountains at 0 and 12 UT with $T' \sim 30-35$ K in Figures 5a and 5b. There are also MWs over the Appalachian Mountains with $T' \sim 10-15$ K at 12 UT (red arrow in Figure 5b) and smaller amplitudes of $T' \sim 2-3$ K at 0 UT (Figure 5a). The phase lines of the MWs are oriented northeast to southwest. Finally, GWs are seen over the *entrance region of the major core* of the polar vortex jet over the northern Atlantic Ocean having phase lines approximately *perpendicular* to the background flow with $T' \sim 10-20$ K (turquoise arrows in Figures 5a and 5b). These phase lines are orientated northwest to southeast. Importantly, these GWs extend from 26 to 53°N over the Atlantic Ocean, and follow the polar vortex jet flow (green lines in Figure 5a). It is extremely unlikely that these entrance region GWs are advected MWs from the Appalachians because (a) the former GWs are strong at 0 UT from 26 to 53°N over the Atlantic Ocean, at which time there is insignificant MWs over the Appalachian Mountains (see Figure 5a), (b) the former GWs are generated as far south as ∼26°N at both 0 and 12 UT, well out of the range that the MWs over the Appalachian propagate (see Figure 5b), (c) the former GWs have phase lines orientated northwest to southeast, opposite to that of the Appalachians MWs (northeast to southwest), (d) the Appalachians MWs do not advect more than ∼10° downstream (eastward) (see the longitude-altitude slice through the Appalachian MWs later in this subsection), and (e) the former GWs are located in a region where theory predicts that the atmosphere extracts energy from the vortex jet shear to generate GWs (see Section 3.4). Therefore, these entrance region GWs (turquoise arrows in Figures 5a and 5b) are a new type of stratospheric jet-generated GWs that has not been previously discussed in the literature (to our knowledge). Movie S3 shows T' at $z = 40$ km for GWs with $\lambda_H < 2{,}001$ km during 11–14 January. Vectors show $(\overline{U},\overline{V})$ at $z = 40$ km. The structure and variability of the entrance/core/exit region GWs and MWs are seen, along with the slow evolution of the polar vortex jet over the 4 day period. Importantly, although the MWs over the Appalachian Mountains only occur sporadically during 11.75–12.6 and 13.25–14.2 January, the entrance region GWs over the Atlantic Ocean (with $T' \sim 10-20$ K) are ubiquitous and omnipresent throughout the entire 4-day period.

At $z = 70$ km in Figures 5c and 5d, the primary GWs generated in the major cores of the polar vortex jet are no longer visible because they have dissipated (see Figures 1 and 2). In their place, we see the secondary GWs generated by MSVC of those primary GWs (green arrows). In addition, the GWs generated in the entrance and exit regions over Asia are still visible at this altitude, although they are beginning to break/dissipate. Finally, the entrance region GWs over the Atlantic Ocean are even stronger at this altitude at both 0 and 12 UT in Figures 5c and 5d. Movie S4 shows T' at $z = 70$ km for GWs with $\lambda_H < 2{,}001$ km from 11 to 14 January. Vectors show $(\overline{U},\overline{V})$ at $z = 70$ km. The entrance region GWs over the Atlantic Ocean with phase lines perpendicular to the wind flow are ubiquitous and omnipresent throughout. The MWs over the Appalachian Mountains, the Alps and the Carpathian Mountains are not visible. Note that the exit/entrance region GWs over Asia are highly variable.

Figure 6 shows T' at $z = 95$ and 120 km. GW dissipation is prevalent throughout the MLT at $z = 95$ km. Some GWs having arc-like and planar structures are seen over Europe (green arrows in Figures 6a and 6b) and Asia. Movie S5 shows T' at $z = 95$ km. We see a complex "soup" of GWs at this altitude. Note the semi-diurnal rotation of the wind at $z = 95$ km due to the semi-diurnal tide (vectors). At $z = 120$ km in Figures 6c and 6d, GWs with planar and arc-like structures occur (a) over the Atlantic Ocean at 20–100°W and 10–60°N (turquoise arrows), (b) over Europe at 0–40°E and 40–70°N (green arrows), and (c) over the northern Asian continent, Arctic Ocean and western Pacific Ocean. These GWs have different characteristics (horizontal scales and propagation directions) than the GWs in Figures 5c and 5d, and are therefore likely higher-order GWs generated/magnified by (i.e., "from") the polar vortex jet. (Here, magnified includes MWs from the Alps, Appalachian Mountains, etc.). Movie S6 shows T' at $z = 120$ km. The GWs often have more coherence at this altitude than at $z = 95$ km (e.g., note the concentric/arc-like GWs over Europe at ∼18 UT on 12 January). Note that the semi-diurnal tide is still the dominant contributor to the background wind at this altitude.

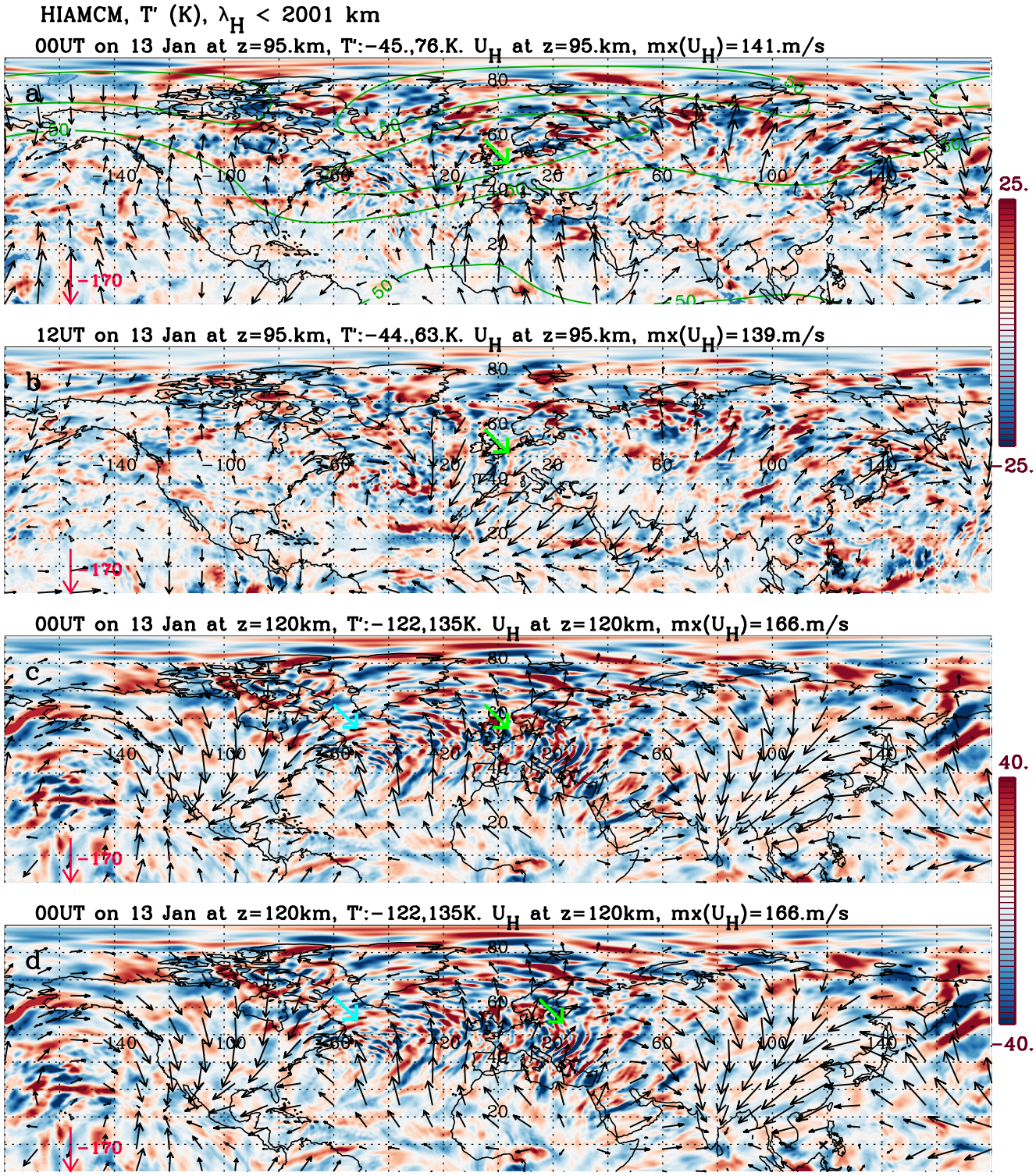

Figure 6. Same as Figure 5, except at z = 95 km (a and b) and z = 120 km (c and d).

Figure 7a shows $T'\left(\overline{\rho}/\rho_0\right)^{0.12}$ for GWs with $\lambda_H < 2{,}001$ km at 50.2° W at 0 UT on 13 January. This longitude cuts through the entrance region of the major core of the polar vortex jet (see Figure 5c). Primary GWs are generated at $z \sim 35-60$ km at $45-55$°N and dissipate at $z \sim 80$ km, as seen in the blow-up region of the entrance of the major core of the polar vortex jet in Figure 7b. At higher altitudes, higher-order GWs are generated at $z \sim 100$ km and

$40-45°$N, some of which propagate to $z = 300$ km (Figure 7a). Figure 7c shows the results at 90.0°E at 0 UT on 13 January, which cuts through the exit region of the major core of the polar vortex jet (see Figure 5). Primary GWs are generated at $z \sim 50-60$ km at $50-80°$N, as shown in Figure 7d. Higher-order GWs are generated at $60-80°$N and $z \sim 120-130$ km, some of which propagate to $z = 300$ km (see Figure 7c). Figure 7e show the results at 135.0°E at 12 UT on 13 January, which cuts through the entrance region of the minor core of the polar vortex jet (see Figure 5). Primary GWs are generated at $z \sim 30-40$ km at $45-65°$N, as shown in Figure 7f. Higher-order GWs are generated at $55-90°$N and $z \sim 120-130$ km, and propagate to $z = 300$ km. Figures 7g and 7h shows the results at 69.7°W at 12 UT on 13 January, which intersects the Appalachian Mountains. Intrinsically northwestward-propagating MWs are observed at $40-45°$N. It is possible that some of the smaller-amplitude higher-order GWs at $20-35°$N and $z \simeq 130-200$ km result from this MW event. Note that GW breaking/dissipation occurs where $|u_H'/(c_H - U_H)| \simeq (0.7-1)$. Here, u_H' is the horizontal wind amplitude of the GW, c_H is the GW horizontal phase speed, and U_H is the projection of the background wind along the GW propagation direction (Fritts & Alexander, 2003; Lindzen, 1981). In general, wave breaking occurs from a combination of background wind changes that cause $c_H - U_H$ to decrease, and near-exponential growth in altitude of u_H'.

Figure 8a shows a longitude-altitude slice of $w'(\overline{\rho}/\rho_0)^{0.3}$ at 43.25°N at 12 UT on 13 January 2016 from the HIAMCM for GWs with $\lambda_H < 2{,}001$ km. This slice captures MWs from orographic forcing over the Appalachian Mountains, the Alps and the Carpathian Mountains (red arrows; dash yellow lines are located at 70°W, 10°E, and 25°E). These MWs have $\lambda_z \sim 5-10$ km and slanted phase lines that can be traced to the ground. The MWs over the Appalachians span 60–80°W and dissipate at $z \sim 60$ km. In addition, GWs with much larger $|\lambda_z| \sim 30-50$ km are seen at $z \sim 40$–80 km over the Atlantic Ocean at 60°W to 10°E (pink arrows). These are the entrance region GWs to the major core of the polar vortex jet (turquoise arrows in Figures 5a and 5b). By following the phase lines down in altitude, it is seen that these GWs are the upper-altitude portion of the X-structure GWs generated by the polar vortex jet (see Figures 16 and 17 of V23); in this case, the approximate center of the X-structure occurs at $z \sim 20-35$ km (purple arrow in Figure 8a). These large-$|\lambda_z|$ entrance region GWs are also seen over the Atlantic Ocean at 50.25°N (pink arrow, dash yellow line at 50°W in Figure 8b) and at 60.25°N (pink arrow in Figure 8c), with X-structure generation regions at $z \sim 20-35$ km indicted with purple arrows in Figures 8b and 8c. In addition, the exit region GWs (from the major core) and entrance region GWs (from the minor core) are seen at 60.25°N at 90°E and 135°E, respectively (dash yellow lines in Figure 8c) (purple and turquoise arrows, respectively, in Figures 5a–5d).

3.2.3. "Magnifying Glass" Effect of the Polar Vortex Jet on the Amplitudes of the Higher-Order GWs

As discussed in Section 1, the polar vortex jet leads to an increased $|\lambda_z|$ within the polar vortex jet of intrinsically westward-propagating GWs, thereby delaying GW breaking until these GWs reach the middle/upper portion of the polar vortex jet. Thus typical slow (intrinsic) westward-propagating GWs deposit their momentum in the lower stratosphere if they propagate outside (poleward or equatorward) of the polar vortex jet, and in the upper stratosphere if they propagate westward intrinsically within the polar vortex jet. (Note that GWs with very small initial amplitudes can propagate to much higher altitudes before breaking, as has been observed (e.g., Fritts et al., 2016)). This locational difference is important because the strength of the resulting LBFs and secondary GW amplitudes are proportional to the primary GW amplitudes squared. In particular, if a primary GW is excited at z_i then dissipates and creates a LBF at z_b (Vadas et al., 2003, 2018), the amplitude of a secondary GW at a given altitude z (whereby $z > z_b$) is proportional to:

$$\text{secondary GW amplitude} \propto \left[e^{(z_b - z_i)/2\mathcal{H}}\right]^2 e^{(z - z_b)/2\mathcal{H}}, \tag{3}$$

(Equation 9 of Vadas & Becker, 2019), where $\mathcal{H}$ is the density scale height. Here we neglect wind effects. The first factor on the right-hand side (RHS) of Equation 3 corresponds to the initial amplitude of a secondary GW generated at z_b, while the second factor gives the usual conservative growth of this secondary GW between z_b and z. The RHS of Equation 3 can be rewritten as (Equation 9 of Vadas & Becker, 2019):

$$\text{secondary GW amplitude} \propto e^{(z - z_i)/2\mathcal{H}} e^{(z_b - z_i)/2\mathcal{H}}. \tag{4}$$

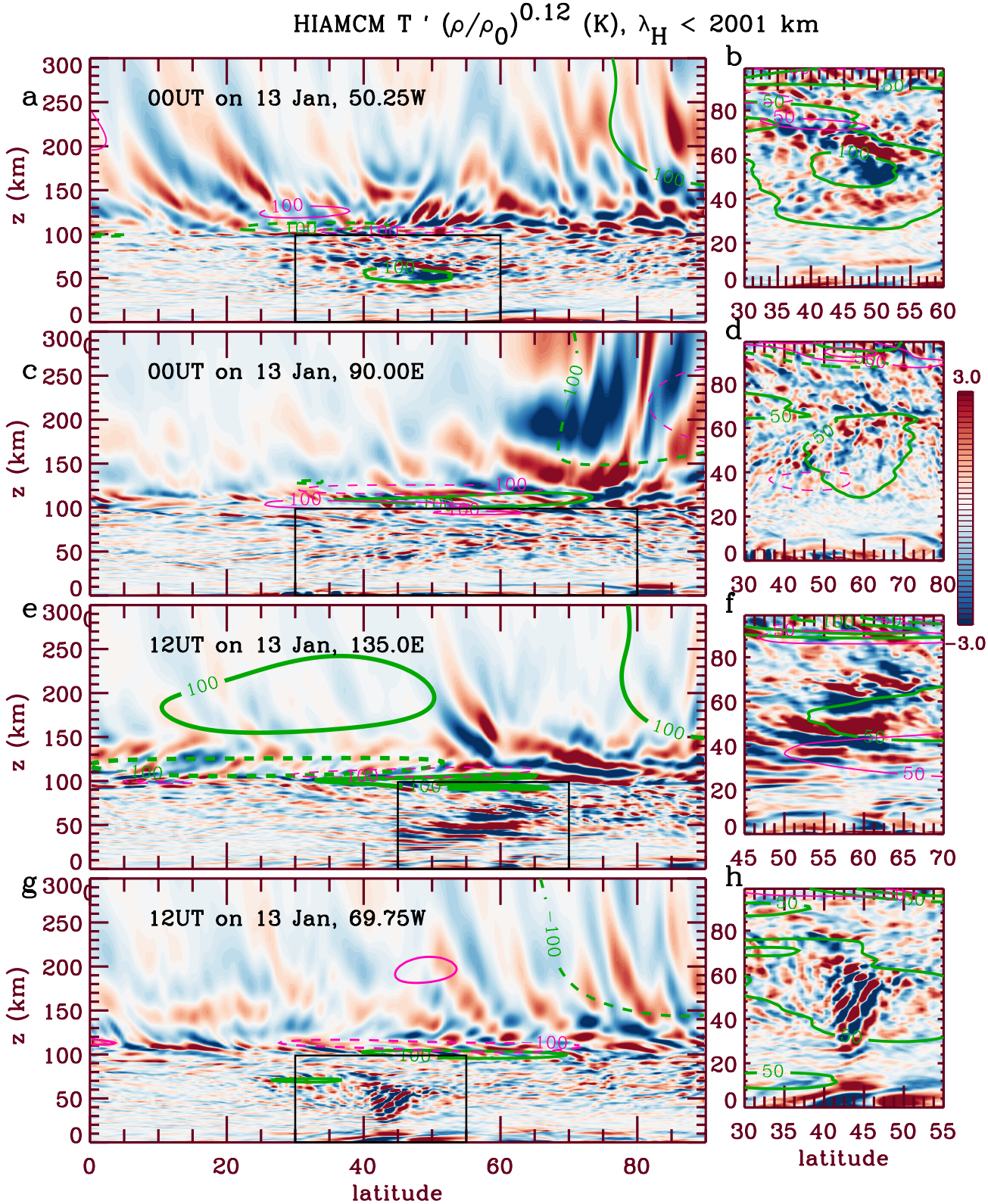

Figure 7. HIAMCM $T'(\overline{\rho}/\rho_0)^{0.12}$ (color, in K) for GWs with λ_H < 2,001 km as functions of latitude and z on 13 January 2016. ρ_0 = 1,191 g/m^3. (a) 50.2°W at 0 UT. (b) Blow up of the black rectangle in (a). Rows 2–4: Same as row 1 but at 90.0°E at 0 UT (row 2), 135°E at 12 UT (row 3) and 69.7°W at 12 UT (row 4). Green and pink lines show $\overline{U}$ and $\overline{V}$, respectively, with solid (dash) lines for positive (negative) values. The contours displayed are: (a, c, e, g) ±100 m/s. (b, d, f, h) ±50 and 100 m/s.

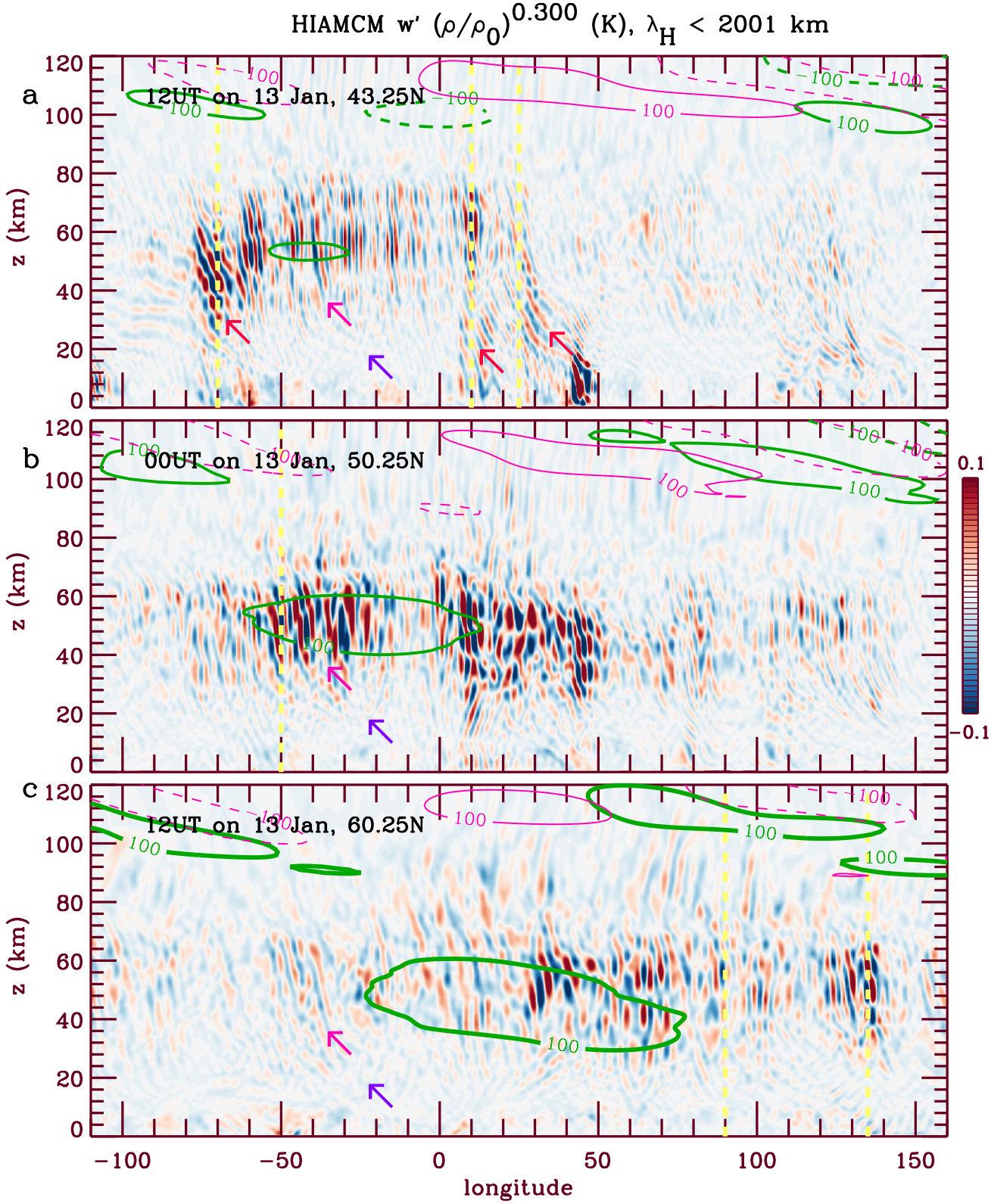

Figure 8.

The first factor on the RHS of Equation 4, $e^{(z-z_i)/2\mathcal{H}}$, describes the amplitude growth of a conservative GW between z_i and z. The second factor, $e^{(z_b-z_i)/2\mathcal{H}}$, increases exponentially with increasing z_b. Thus the higher the altitude of the LBF, the larger the amplitudes of the secondary GWs at z. Therefore, if identical intrinsic westward-propagating GWs are excited 1) outside of the polar vortex jet ("case #1") or 2) directly below the polar vortex jet ("case #2"), then the case #1 GWs will create a LBF lower in altitude than that from the case #2 GWs. Although the atmosphere generates secondary GWs in both cases, the amplitudes of the secondary GWs in case #2 will be much larger than those in case #1 at a given higher altitude z. Since the next higher-order GW amplitudes are proportional to the previous (e.g., secondary) GW amplitudes squared, the amplitudes of the higher-order GWs from case #2 will be much larger than those from case #1. Thus the polar vortex jet acts like a "magnifying glass" by exponentially increasing the amplitudes of the higher-order thermospheric GWs which arise from the primary GWs that propagate through the polar vortex jet (as compared with those that do not). This is likely an important reason why the amplitudes of the wintertime GWs in the stratosphere, mesosphere and thermosphere correlate well with the strength of the polar vortex jet (Becker, Goncharenko, et al., 2022; Frissell et al., 2016; Harvey et al., 2023).

3.2.4. Higher-Order GWs in the Thermosphere From the Polar Vortex Jet

Figure 9a shows T' at $z = 200$ km for GWs with $\lambda_H < 2{,}001$ km at 17 UT on 12 January centered on northern North America, while Figure 9b shows the same time centered on northern Europe. Higher-order GWs radiate away from Europe (green arrows). Those which travel northwestward away from Europe propagate over the high-latitude Arctic region (e.g., Greenland), then southward over the continental US (CONUS) due to the favorable northward background wind over the CONUS at that time. Such GWs could be misidentified as being generated by auroral activity because of their southward propagation at local time (LT) noon, their horizontal wavelengths, and their apparent source location in the Arctic region.

Figure 10 shows T' at $z = 200$ km every 6 hr from 6 UT on 12 January to 12 UT on 13 January for GWs with $\lambda_H < 2{,}001$ km. Vectors show $(\overline{U}, \overline{V})$ at $z = 200$ km; this wind mainly reflects the horizontal wind component of the diurnal tide. Higher-order GWs with concentric ring/arc-like structures propagate away from the entrance, core and exit regions of the polar vortex jet. Those that propagate over the Arctic propagate southward over the CONUS at 18 UT on 12 January and 0 UT on 13 January with $T' \sim 20 - 30$ K and $\lambda_H \sim 200 - 2{,}000$ km (see Figures 10c and 10d). At 0 UT on 13 January (Figure 10d), higher-order concentric GWs propagate west, northwest, north and northeastward away from Europe because the background wind is southeastward then. Note that the southeastward-propagating GWs seen at $z = 120$ km at this time in Figures 6c and 6d are mostly filtered out here because the intervening background wind is southeastward (see Figure 10d). "Wind filtering" occurs because GWs that propagate in the same direction as the wind have reduced $|\lambda_z|$, which causes them to more-easily break and/or dissipate from molecular viscosity (Becker & Vadas, 2020; Fritts & Vadas, 2008; Lund & Fritts, 2012; Vadas, 2007). (Note that GW dissipation in the thermosphere creates LBFs that further generate upward and downward-propagating higher-order GWs (e.g., Vadas & Liu, 2009, 2013). Possible evidence of downward-propagating GWs (upward phases in time) is seen above ALOMAR at $z \sim 120 - 180$ km in Figure 1a.) At 6 UT on 12 and 13 January (Figures 10a and 10e), higher-order concentric GWs propagate northwest, north and northeastward over the northern Atlantic Ocean/Greenland region because the background wind is southward then. These GWs likely arise from the dissipation of secondary GWs from the entrance region of the major vortex jet, as well as occasionally from the dissipation of secondary GWs generated by MW breaking over the Appalachian Mountains (e.g., Vadas & Becker, 2019). In addition, higher-order GWs with arc-like structures over the exit region of the major vortex jet and from the entrance/core regions of the minor vortex jet are seen in Figure 10.

In general, the GWs with the largest amplitudes in Figure 10 propagate against the background wind, in agreement with model results (Becker, Goncharenko, et al., 2022) and observations (Crowley & Rodrigues, 2012; Crowley

Figure 8. $w'(\overline{\rho}/\rho_0)^{0.3}$ (color, in K) from the HIAMCM for GWs with $\lambda_H < 2{,}001$ km as functions of longitude and z on 13 January 2016. $\rho_0 = 1{,}185$ g/m^3. (a) 43.25°N at 12 UT. The yellow dash lines show 70°W, 10°E, and 25°E. (b) 50.25°N at 0 UT. The yellow dash line shows 50°W. (c) 60.25°N at 12 UT. The yellow dash lines show 90°E and 135°E. Green and pink lines show $\overline{U}$ and $\overline{V}$, respectively in ±100 m/s contour intervals, with solid (dash) lines showing positive (negative) values. Red arrows show MW events, pink arrows show entrance region GWs, and purple arrows indicate the "X-structure" primary GWs from the polar vortex jet.

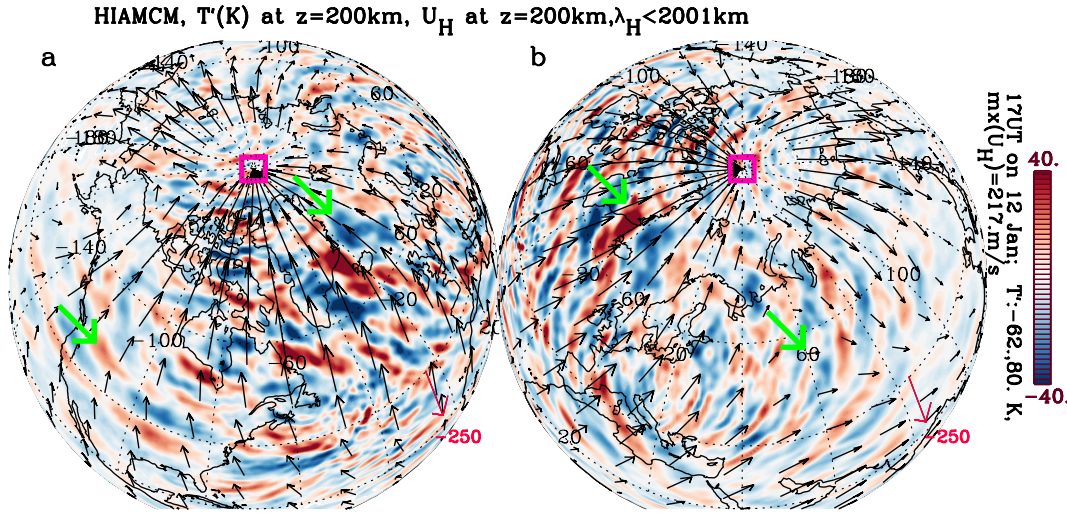

Figure 9. T' (colors, in K) at $z = 200$ km at 17 UT on 12 January 2016 for GWs with $\lambda_H < 2{,}001$ km from the HIAMCM for 2 different perspectives centered on northern North America (a) and northern Europe (b). Vectors show $(\overline{U},\overline{V})$ at $z = 200$ km. The downward red arrow in the lower right-hand corner of each panel shows $\overline{V} = -250$ m/s. Minimum and maximum values of T' and the maximum value of $\overline{U}_H = \sqrt{\overline{U}^2 + \overline{V}^2}$ are given in the caption. The colors are oversaturated somewhat to see the GWs. Green arrows show higher-order GWs from the core of the major vortex jet. The pink square shows the north pole.

et al., 1987; Xu et al., 2024). Since the background wind rotates clockwise from the western to eastern part of each map in Figure 10 (which covers a 24 hr LT change), the GW propagation direction also rotates clockwise from the western to eastern part of each map (although with a ∼180° phase shift from the background wind direction). Additionally, at a given mid-latitude northern hemisphere location on the map (e.g., over Europe), the background wind generally rotates clockwise in LT throughout the day, which results in the GW propagation direction also rotating clockwise in LT (although again with a ∼180° phase shift).

Movie S7 shows T' at $z = 200$ km for GWs with $\lambda_H < 2{,}001$ km every hour from 11 to 14 January. Vectors show $(\overline{U},\overline{V})$ at $z = 200$ km. The clockwise rotation of the GW propagation direction in LT is apparent. The strongest GW amplitudes occur during LT late morning, noon and afternoon when the tidal flow is strongly poleward (Figure 9 of Becker, Goncharenko, et al., 2022). Higher-order GWs from the major core of the polar vortex jet contribute significantly to the GW activity in the thermosphere at mid and high latitudes at all times. Higher-order GWs from the entrance and exit regions of the major vortex jet contribute daily to the GW activity at ∼6–17 UT and ∼20–31 UT, respectively. Higher-order GWs from the entrance/core regions of the minor vortex jet contribute daily at ∼18–21 UT. Importantly, some higher-order GWs from Europe propagate over the Arctic region then southward over the CONUS to $\sim 15 - 20$°N daily at $\sim 14 - 24$ UT ($\sim 9 - 16$ LT). Because these GWs are far from their source, they generally have planar structure over the CONUS. Such extensive propagation is possible at these times because the background wind over the CONUS is strongly poleward (northward) then. Movie S8 shows T' every 10 min over Europe/Atlantic Ocean from 60°W to 60°E at $z = 200$ km for GWs with $\lambda_H < 2{,}001$ km during 11–14 January. GWs with concentric ring and arc-like structures radiate away from Europe at most times. Typical parameters for the GWs over Europe are $T' \sim 20 - 60$ K, $\lambda_H \sim 200 - 500$ km, $c_H \sim 160 - 200$ m/s, and $\tau_r \sim 20$ min to 1 hr. Movie S9 shows T' over the CONUS at $z = 200$ km for GWs with $\lambda_H < 2{,}001$ km every 10 min during 11–14 January. Typical parameters for the southward-propagating GWs over the CONUS (at $\sim 14 - 24$ UT daily) are $T' \sim 20 - 40$ K, $\lambda_H \sim 200 - 2{,}200$ km, $c_H \sim 165 - 260$ m/s, and $\tau_r \sim 20$ min to 2.4 hr.

Figure 11 shows T' at $z = 250$ km during 11–14 January for GWs with $\lambda_H < 2{,}001$ km. The left, middle and right columns are centered over the Atlantic Ocean at 8 UT, over Europe at 0 UT, and over the Asian continent at 16 UT. Higher-order GWs with concentric ring/arc-like structures radiate away from the entrance region of the major polar vortex jet (left column), from the core of the major polar vortex jet (middle column), and from the exit region of the major polar vortex jet and entrance/core regions of the minor polar vortex jet (right column).

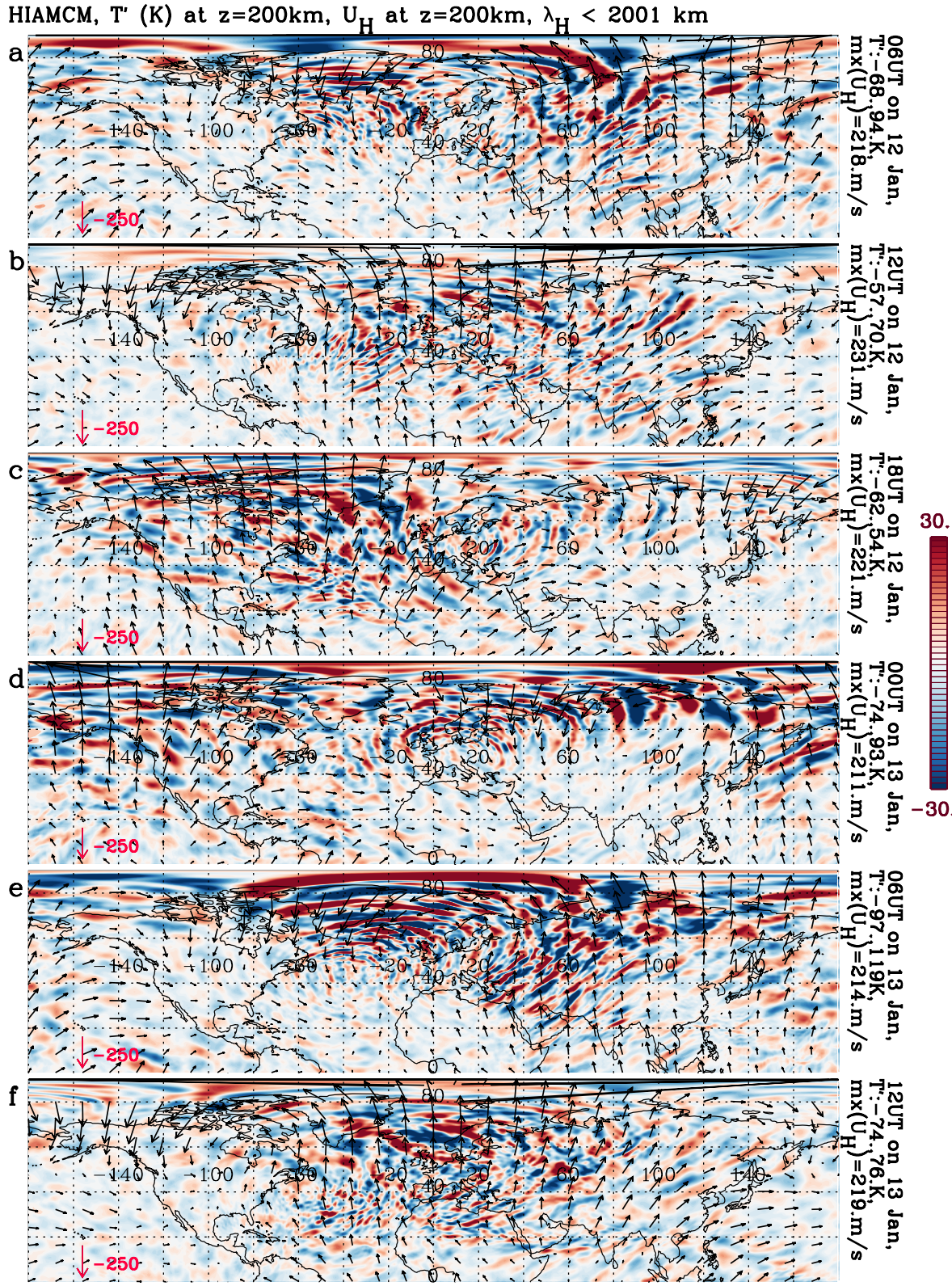

Figure 10. T' (colors, in K) at $z = 200$ km every 6 hr from 6 UT on 12 January to 12 UT on 13 January 2016 for GWs with $\lambda_H < 2{,}001$ km from the HIAMCM. Vectors show $(\overline{U}, \overline{V})$ at $z = 200$ km. The downward red arrows in the lower left-hand corners show $\overline{V} = -250$ m/s. Minimum and maximum values of T' are given in each caption. The colors are oversaturated to see the GWs.

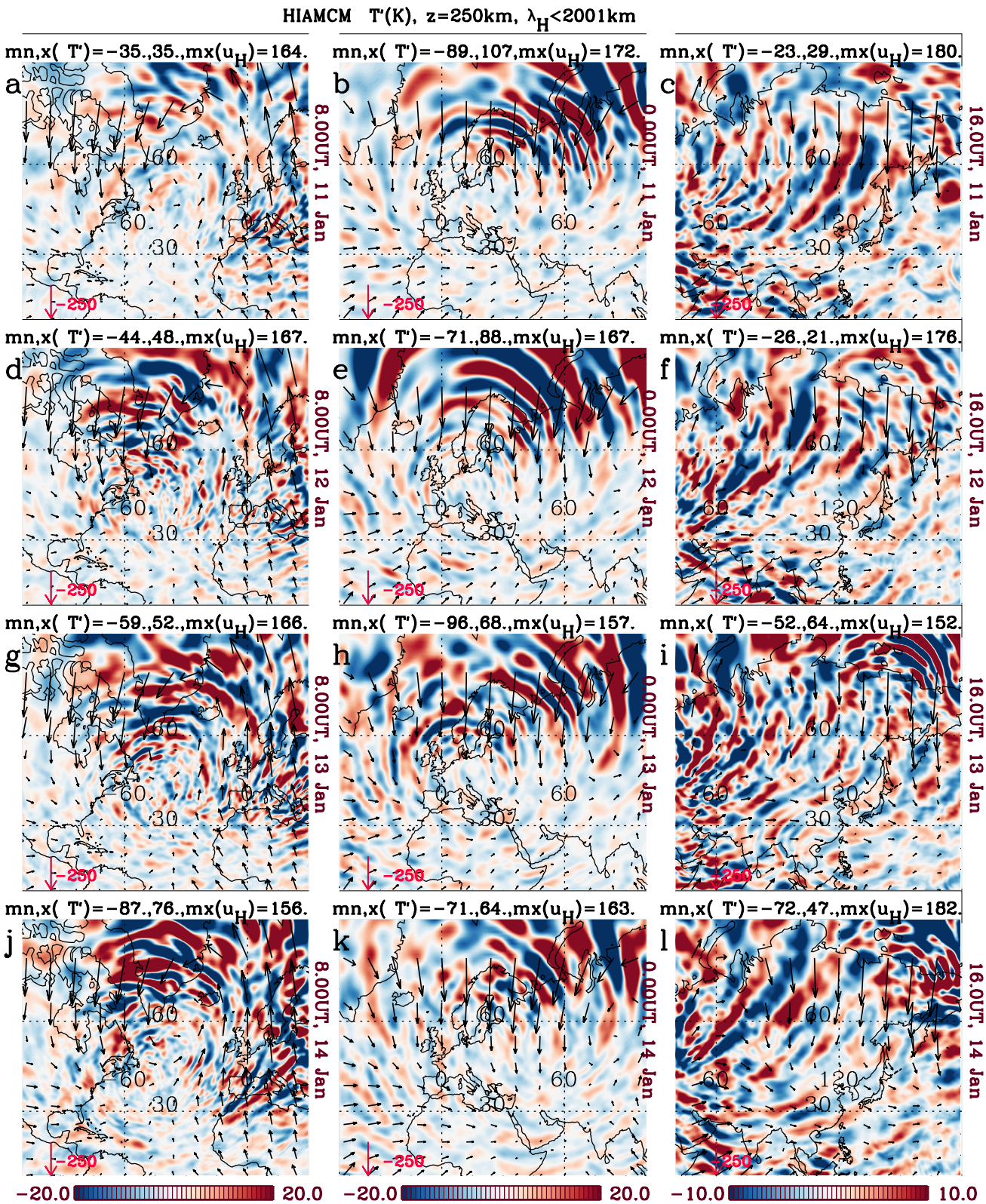

Figure 11. T' (colors, in K) at $z = 250$ km for GWs with $\lambda_H < 2{,}001$ km. Rows 1–4 show 11–14 January 2016, respectively. Columns 1–3 show the Atlantic Ocean sector at 8 UT, the European sector at 0 UT, and the Asian sector at 16 UT, respectively. Vectors show $(\overline{U}, \overline{V})$ at $z = 250$ km. The downward red arrow in the lower left-hand corner of each panel shows $\overline{V} = -250$ m/s. Minimum and maximum values of T' are given in each caption. The colors are oversaturated to see the GWs.

3.3. Large-Scale Higher-Order GWs From the Polar Vortex Jet

Figure 12 shows T' at $z = 200$ km for large-scale GWs with $2{,}001 < \lambda_H < 4{,}447$ km every 6 hr from 6 UT on 12 January to 12 UT on 13 January in the northern hemisphere. Large-scale, large-amplitude GWs with $T' \sim 20$–50 K are ubiquitous in the mid-thermosphere and originate at mid to high latitudes. These large-scale GWs occur daily around LT noon, and propagate southwestward where the background wind from the diurnal tide is north/northeastward; thus the morphology of these global GW packets is determined by the morphology of the diurnal tide. There are also weaker large-scale GWs at 12–18 UT over the Pacific Ocean with northeast to southwest phase fronts (Figures 12b and 12c) which create "checkerboard" (red-blue-red) patterns in T' from constructive/destructive interference.

Movie S10 shows T' at $z = 200$ km for large-scale GWs with $2{,}001 < \lambda_H < 4{,}447$ km. The large-scale GWs propagate southwestward across the northern hemisphere daily at ~8–16 LT, with significant day-to-day variability. Typical parameters are $T' \sim 20 - 40$ K, $\lambda_H \sim 3{,}000$ km, $c_H \sim 650$ m/s, and $\tau_r \sim 1.3$ hr. Such fast GWs cannot exist in the troposphere/stratosphere/mesosphere, because they propagate faster than the sound speed there (Vadas et al., 2019). Note that the weaker large-scale GWs over the Pacific Ocean propagate northwestward from the southern hemisphere. Movie S11 shows T' at $z = 80$ km for GWs with $2{,}001 < \lambda_H < 4{,}447$ km. The large-scale, southwestward-propagating GWs are absent at this altitude, thereby verifying that they are created at $z > 80$ km. Further investigation shows that these GWs are created at $z \sim 100 - 110$ km (not shown), which agrees with Figure 3b.

Figure 13 shows snapshots of T' at $z = 130$ km for GWs with $2{,}001 < \lambda_H < 4{,}447$ km at 06 UT and 12 UT on 12 January. Large-scale, southwestward-propagating GWs with partial concentric ring/arc-like structures are seen at high latitudes over Europe and Asia.

3.4. Generation and Amplification of GWs by the Polar Vortex Jet

Becker, Vadas, et al. (2022) derived an expression for the generation/amplification of "mesoscale" (i.e., medium-scale) GWs in a background flow that is assumed to include only geostrophic components. This formalism applies, for example, for the generation/amplification of GWs by the horizontal and vertical wind shear of the polar vortex jet, and is valid at $2 \text{ km} \le z \le 80$ km. (Above $z = 80$ km, the tides become the dominant large-scale flow, but these waves cannot be approximated as a geostrophic flow.) Here, the horizontal scales of the GWs are assumed to be significantly smaller than that of the large-scale background flow. The relevant expression for our purpose from Becker, Vadas, et al. (2022) is the so-called mesoscale kinetic energy source or "MKS" equation (their Equation B22):

$$\begin{aligned} \text{MKS} = & -\left[\overline{(v')^2} - \overline{(u')^2}\right]\frac{\partial \overline{V}_g}{\partial y} - \overline{u'v'}\left[\frac{\partial \overline{V}_g}{\partial x} - \frac{\partial\left(\cos\theta \overline{U}_g\right)}{\cos\theta \ \partial y} + 2\frac{\partial \overline{U}_g}{\partial y}\right] \\ & -\overline{\left(u'w'\right)}\frac{\partial \overline{U}_g}{\partial z} - \overline{\left(v'w'\right)}\frac{\partial \overline{V}_g}{\partial z}, \end{aligned} \tag{5}$$

where primes denote the GWs, (u', v', w') is the zonal, meridional and vertical wind perturbations due to the mesoscale GWs, $\overline{U}_g, \overline{V}_g$ are the zonal and meridional components of the background geostrophic wind (which is the large-scale wind that blows along constant pressure surfaces in z coordinates), $\xi_g = \partial \overline{V}_g/\partial x - (\cos\theta)^{-1}\partial\left(\cos\theta \overline{U}_g\right)/\partial y$ is the large-scale relative vorticity in spherical coordinates,

$$\frac{\partial}{\partial x} = \frac{1}{\mathrm{R_E}\cos\theta}\frac{\partial}{\partial \phi}, \qquad \frac{\partial}{\partial y} = \frac{1}{\mathrm{R_E}}\frac{\partial}{\partial \theta}, \tag{6}$$

ϕ is longitude, θ is latitude, and $\mathrm{R_E}$ is the Earth's radius. Energy is extracted from the geostrophic wind shear via shear production when

$$\text{MKS} > 0, \tag{7}$$

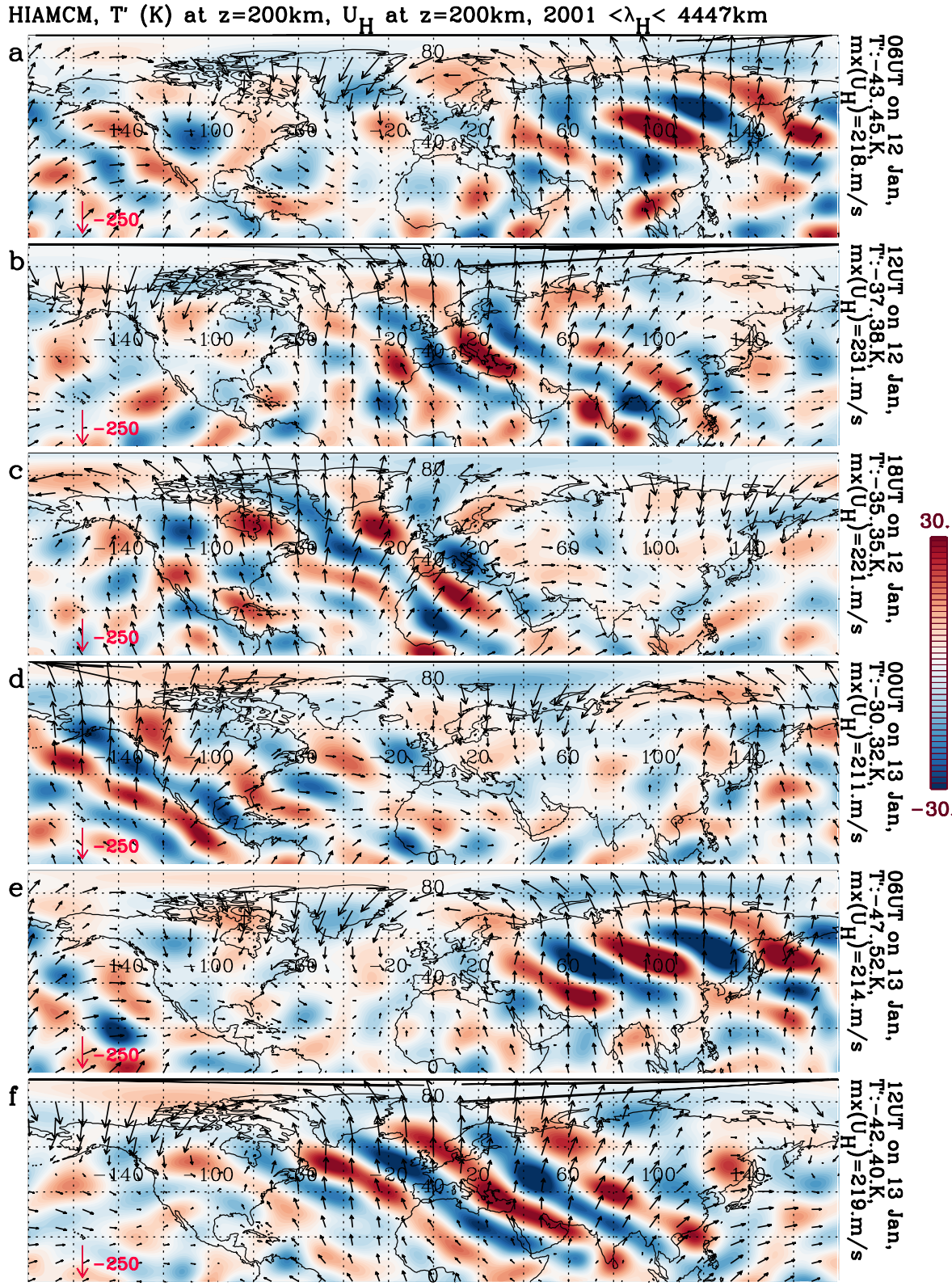

Figure 12. Same as Figure 10 but for GWs with 2,001 < λ_H < 4,447 km.

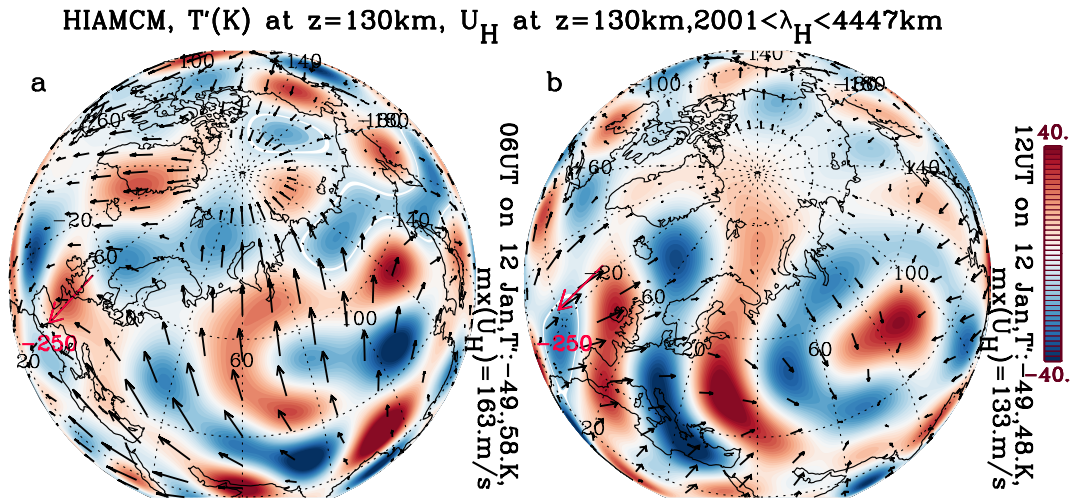

Figure 13. T' (colors, in K) at $z = 130$ km at 6 UT (a) and 12 UT (b) on 12 January 2016 for GWs with $2{,}001 < \lambda_H < 4{,}447$ km from the HIAMCM. Vectors show $(\overline{U}, \overline{V})$ at $z = 130$ km. The downward red arrow in the lower left-hand corner of each panel shows $\overline{V} = -250$ m/s. Minimum and maximum values of T' are given in each caption. The colors are somewhat oversaturated to see the GWs.

(Becker, Vadas, et al., 2022) for which existing GWs are amplified. (Note: the GWs generated/amplified by this "spontaneous emission" process are not secondary GWs from LBFs.) The third and forth terms of Equation 5 (i.e., $-\overline{(u'w')}\partial\overline{U}_g/\partial z$ and $-\overline{(v'w')}\partial\overline{V}_g/\partial z$, respectively), are the most important terms for GW generation in the core of the polar vortex jet (V23). Since $\nabla.\mathbf{V_g} = 0$, and assuming that the vertical velocity of the geostrophic flow is approximately zero,

$$\frac{\partial\overline{U}_g}{\partial x} \simeq -\frac{1}{\cos\theta}\frac{\partial(\cos\theta\overline{V}_g)}{\partial y} = -\frac{\partial\overline{V}_g}{\partial y} + \frac{\tan\theta\overline{V}_g}{\mathrm{R_E}}. \tag{8}$$

Since the large-scale flow, $(\overline{U}, \overline{V})$, contains waves with $\lambda_H > 4{,}447$ km, nearly all large-scale inertia GWs have been removed. Hence, outside the tropics (i.e., for $|\theta| \geq 20 - 30°$) at $z = 2 - 80$ km, we have to a very good approximation that

$$\overline{U}_g \simeq \overline{U} \quad \text{and} \quad \overline{V}_g \simeq \overline{V}. \tag{9}$$

Figure 14 shows the third and forth terms of Equation 5 for GWs with $\lambda_H < 2{,}001$ km at 0 UT on 13 January at $z = 40$, 55, and 70 km. Here we have set $\overline{U}_g = \overline{U}$ and $\overline{V}_g = \overline{V}$ from Equation 9. The overlines denote horizontal averaging over 700 km × 700 km. We do not show the first and second terms of Equation 5 because they have negligible amplitudes except over Europe at $z = 55$ km whereby MKS > 0 for the second term. GW generation/amplification occurs in regions where the sum of the third and forth terms is >0 from Equation 7. GW generation/amplification occurs (a) in the core of the major vortex jet at $z = 40$ km, primarily from the vertical shear of the meridional wind (see Figure 14d); (b) in the entrance region of the major vortex jet at $z = 55$ km ($z = 70$ km) from the vertical shear of the zonal (meridional) wind (Figures 14b and 14f); (c) in the exit region of the major vortex jet and in the entrance/core regions of the minor vortex jet at $z = 55$ km for the vertical shear of the zonal and meridional wind (Figures 14b and 14e). Comparing with Figure 5, the GW generation/amplification regions predicted from MKS analysis coincide with the locations of the primary GWs "from" (i.e., generated/amplified by) the entrance, core and exit regions of the polar vortex jet.

3.5. Potential Energy Density of the Gravity Waves

The potential energy density per unit mass (PE) of the GWs is

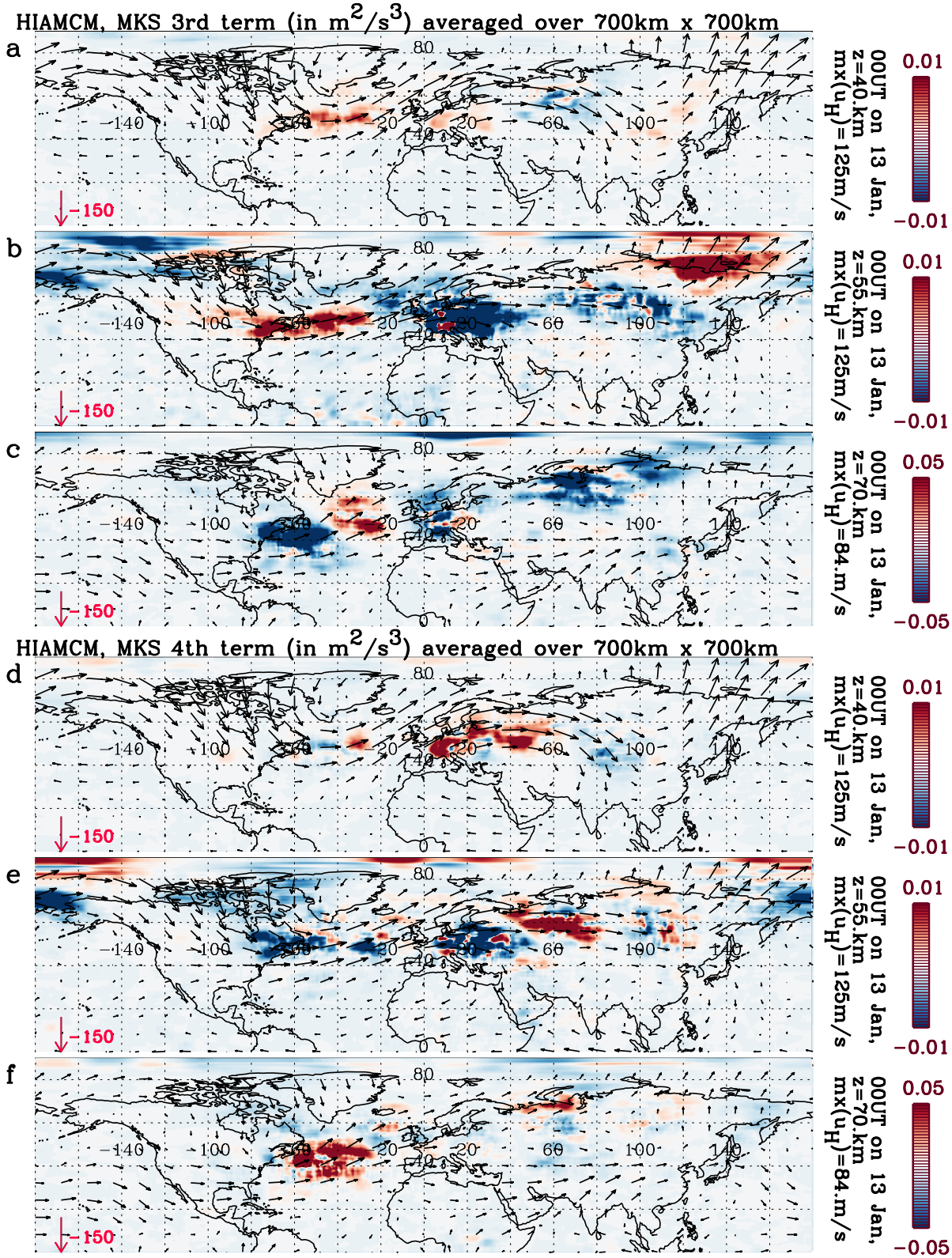

Figure 14. (a–c): Third term of Equation 5, $-\overline{(u'w')}\partial\bar{U}_g/\partial z$ (in m^2/s^3), at $z = 40$, 55, and 70 km at 0 UT on 13 January for GWs with $\lambda_H < 2{,}001$ km from the HIAMCM. The overlines denote horizontal averaging over 700 km × 700 km. (d–f) Same as (a–c), but for the forth term of Equation 5, $-\overline{(v'w')}\partial\bar{V}_g/\partial z$. Vectors show $(\overline{U},\overline{V})$ at each altitude. The downward red arrows in the lower left-hand corners show $\overline{V} = -150$ m/s. Maximum values of $\bar{U}_H = \sqrt{\bar{U}^2 + \bar{V}^2}$ are given in each caption.

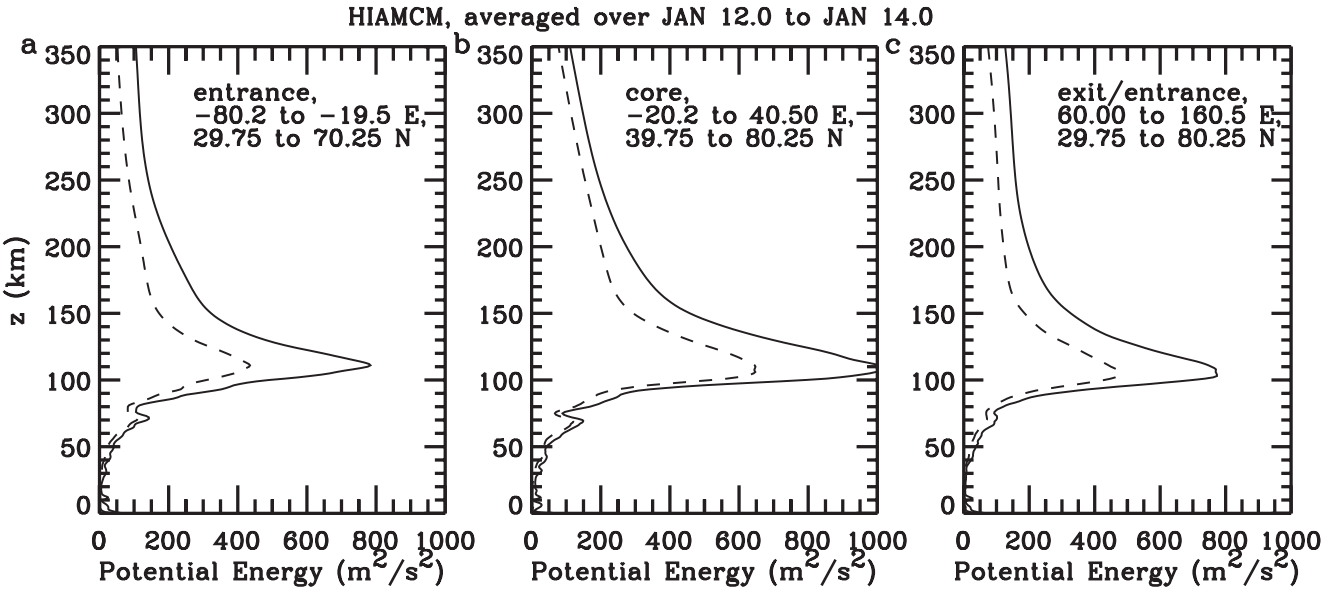

Figure 15. (a) Potential energy (PE) for the GWs with $2{,}001 < \lambda_H < 4{,}447$ km (solid line) and with $\lambda_H < 2{,}001$ km (dashed line) from the HIAMCM. The PE is averaged from 12.0 to 14.0 January 2016 over the entrance region of the major vortex jet at 20–80°W and 30–70°N. (b) Same as (a), but over the core of the major vortex jet at 20°W–40°E and 40–80°N. (c) Same as (a), but over the exit region of the major jet and the entrance region of the minor jet at 60–160°E and 30–80°N.

$$\mathrm{PE} = \frac{1}{2}\left(\frac{g}{N_B}\right)^2\left(\frac{T'}{\overline{T}}\right)^2, \tag{10}$$

where $N_B = 2\pi/\tau_B$ is the buoyancy frequency and g is the gravitational acceleration. We approximate

$$N_B{}^2 \simeq g^2/(C_p\overline{T}), \tag{11}$$

where $C_p = \gamma r/(\gamma - 1)$, $r = 8{,}308/\mathrm{X_{MW}}$ m^2 s^{-2} K^{-1} and $\mathrm{X_{MW}}$ is the mean molecular weight of a molecule in the gas (in g/mole). We use empirical expressions for γ and $\mathrm{X_{MW}}$:

$$\mathrm{X_{MW}} = \frac{1}{2}(\mathrm{X_{MW0}} - \mathrm{X_{MW1}})\left(1 - \tanh\left(\frac{\mathrm{s} - \mathrm{a}}{\Delta_a}\right)\right) + \mathrm{X_{MW1}}, \tag{12}$$

$$\gamma = \frac{1}{2}(\gamma_0 - \gamma_1)\left(1 - \tanh\left(\frac{\mathrm{s} - \mathrm{b}}{\Delta_b}\right)\right) + \gamma_1, \tag{13}$$

(Equations 3 and 4 of Vadas, 2007), where $\mathrm{s} = -\ln(\overline{\rho})$ ($\overline{\rho}$ has units of g/m^3), $\mathrm{X_{MW0}} = 28.9$ gm/mole, $\mathrm{X_{MW1}} = 16$ gm/mole, a = 14.9, $\Delta_a = 4.2$, $\gamma_0 = 1.4$, $\gamma_1 = 1.67$, b = 15.1 and $\Delta_b = 4.0$. The decrease of $\mathrm{X_{MW}}$ and increase of γ in altitude is caused by the change from diatomic N_2 and O_2 to monatomic O in the thermosphere.

Figure 15 shows the average PE during 12–14 January as a function of altitude for the HIAMCM GWs in the entrance (Figure 15a) and core (Figure 15b) regions of the major vortex jet and in the exit region of the major vortex jet and the entrance region of the minor vortex jet (Figure 15c). In all three regions, the PE increases exponentially in z at $z \sim 50$–70 km due to the amplitude growth of the primary GWs, decreases at $z \sim 70 - 80$ km due to the dissipation of the primary GWs, increases exponentially again at $z \sim 80 - 110$ km due to the growth of the secondary GWs, then decreases at $z > 110$ km. We note that the altitudinal behavior shown in Figure 15b over the core of the major polar vortex jet is consistent with the snapshot shown in Figure 3a, although Figure 15b is averaged over 20°W–40°E and 40–80°N from 12 to 14 January.

The primary GWs in Figure 15 peak at $z \sim 70$ km. This is consistent with past northern hemisphere results, which found the peak to occur at $z \sim 65 - 70$ km from model results and MF radar observations (Figure 10 of Avsarkisov

et al., 2022). Note that this peak altitude is ∼16 km lower than the simulated primary GW peak over the winter Southern Andes of $z \sim 86$ km (Figure 20 of Vadas & Becker, 2019). The latter southern hemisphere peak altitude of $z \sim 86$ km was verified by winter lidar data at McMurdo Station (Figure 4 from Chu et al., 2022).

In addition, we note from Figure 15 that the decrease of the PE at $z > 110$ km is different from the results of a previous model study of a strong wintertime MW event over the Southern Andes, whereby the PE increased at $z \sim 120 - 150$ km (Figure 20 of Vadas & Becker, 2019). (In that case, the PE behaved in a similar manner at $z < 110$ km). Possible reasons for the difference in the PE at $z > 110$ km are (a) the MWs in that study were highly localized over the Southern Andes up to $z \sim 85$ km, whereas the primary GWs from the polar vortex jet in our current study are localized only up to $z \sim 65$ km, thereby leading to enhanced horizontal spreading of the secondary and higher-order GWs outside the averaged regions in our current study; (b) the MW event over the Southern Andes was approximately twice as energetic (PE $\sim$ 1,600 m^2/s^2 at $z \sim 110$ km) as the polar vortex jet event simulated here, thus yielding larger amplitudes for the higher-order GWs at $z > 110$ km in that case; and (c) the vertical grid spacing in the lower thermosphere was larger in Vadas and Becker (2019) than here, thereby likely biasing some of the tertiary GWs in that study to larger λ_z which are less prone to dissipation (Vadas, 2007).

3.6. Large-Scale LBFs Generated by the Dissipation of Secondary GWs

As discussed above, the dissipation of secondary GWs generated/magnified by the polar vortex jet creates spatially and temporally localized, horizontal LBFs. These LBFs may create the higher-order GWs shown in Figures 10 and 11. We now investigate this possibility. The zonal and meridional LBFs (per unit mass), (F_x, F_y), are the convergence of the vertical flux of the zonal and meridional momentum (e.g., Achatz, 2022):

$$F_x = -\frac{1}{\overline{\rho}}\frac{\partial\left(\overline{\rho u' w'}\right)}{\partial z} \qquad F_y = -\frac{1}{\overline{\rho}}\frac{\partial\left(\overline{\rho v' w'}\right)}{\partial z}, \tag{14}$$

respectively, where the overlines denote averaging in space and time over the GW scales.

We compute the zonal and meridional momentum fluxes, $\overline{\rho u' w'}$ and $\overline{\rho v' w'}$, respectively, for GWs with $\lambda_H < 2{,}001$ km. We then perform a running mean smoothing over 800 km × 800 km horizontally and $\Delta z = 3$ km vertically. Finally we calculate F_x and F_y from Equation 14. Note that performing a running mean smoothing over smaller spatial and temporal scales result in the LBFs that generate the medium-scale GWs (e.g., Figures 10 and 11) (not shown). Figure 16 shows the large-scale LBFs (vectors show (F_x, F_y)) at $z = 110$ km every 6 hr from 0 UT on 12 January to 0 UT on 13 January. The largest-amplitude LBFs occur over Europe at nearly all times. Smaller-amplitude LBFs occur at most northern-hemisphere locations at various times, including over the Atlantic and Pacific Oceans, North America and Asia. We overplot T' at $z = 124$ km for the large-scale GWs with $2{,}001 < \lambda_H < 4{,}447$ km (colors). A complex mix of GWs propagating in different directions occurs, giving rise to blue-red-blue "checkerboard" patterns. In general, enhanced GW activity occurs near the LBFs, for example, propagating away from Europe in Figures 16a, 16c, 16d, and 16e, over the Atlantic Ocean in Figure 16d, and over the Pacific Ocean in Figure 16e. Note that wind filtering/viscous dissipation of the GWs in Figure 16 between $z = 124$ and 200 km causes mainly the southwestward-propagating GWs to survive at $z = 200$ km (compare with Figure 12). Such dissipation may significantly affect the background wind there.

Movie S12 shows the large-scale LBFs at $z = 110$ km (vectors) for 11–14 January. Green lines show LBF magnitudes of 10 and 20 m/s/h at $z = 110$ km. At a given location, the LBFs rotate clockwise twice per day. This rotation is caused by the strong semidiurnal tides in the MLT (see Section 4.3), which filter the secondary GWs propagating upward from below. The location where the LBFs are maximum moves westward from Asia to North America; however, the largest-amplitude LBFs occur over Europe and Asia. The large-scale GWs at $z = 124$ km (T', colors, in K) often have the largest amplitudes near the LBFs. Note that T' exhibits a "checkerboard" appearance at this altitude due to the constructive/destructive interference of GW packets from different sources.

4. Comparison of Data With Simulation Results

We now compare the GWs and winds in the MLT simulated by the HIAMCM with those observed by AIRS, VIIRS/DNB, and meteor radars. These comparisons are important for validating the HIAMCM and the physical

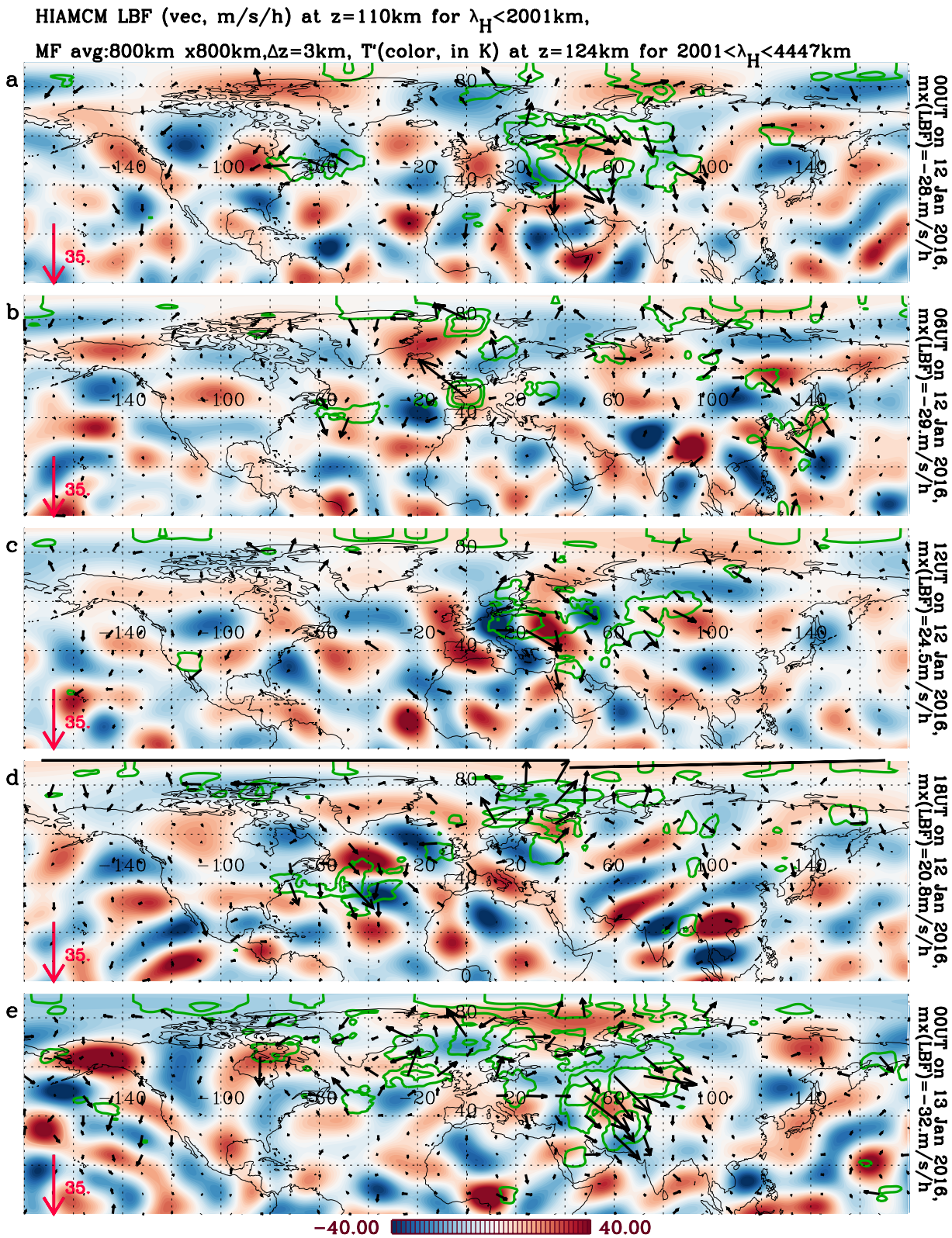

Figure 16. Row 1: $-\overline{\rho}^{-1}\partial(\overline{\rho u' w'})/\partial z$ and $-\overline{\rho}^{-1}\partial(\overline{\rho v' w'})/\partial z$ (vectors, in m/s/h) at $z = 110$ km at 0 UT on 12 January 2016. The momentum fluxes are calculated for GWs with $\lambda_H < 2{,}001$ km from the HIAMCM, and are running-mean averaged over 800 km × 800 km and $\Delta z = 3$ km. Green lines show LBF magnitudes of 10 and 20 m/s/h at $z = 110$ km. The downward red arrows in the lower left-hand corners show 35 m/s/h. T' (colors, in K) are shown at $z = 124$ km at the same time for GWs with $2{,}001 < \lambda_H < 4{,}447$ km from the HIAMCM. Row 2–5: Same as row 1 except at 12.25, 12.5, 12.75, and 13.0 January, respectively.

processes contained therein, including the all-important transfer of momentum and energy throughout the Earth's atmosphere via MSVC of GWs.

4.1. Comparison of AIRS GWs With the Simulated GWs in the Stratosphere

We now compare the HIAMCM GWs in the entrance, core and exit regions of the polar vortex jet with those measured by AIRS (Eckermann et al., 2019; Gong et al., 2012; Hoffmann & Alexander, 2009). Temperature perturbations are retrieved from AIRS using a 4th order polynomial detrending in the cross-track direction (which is approximately zonally) at each altitude, and are interpolated onto a 0.5° grid in latitude and longitude. The left column of Figure 17 shows horizontal slices of T' from the HIAMCM at various altitudes from $z = 42$–51 km and at various times on 13 January. GWs are seen over Europe in the core of the major vortex jet north of 50°N, and from orographic forcing over the Alps and Carpathian Mountains (mainly south of 50°N) in Figure 17a. GWs are seen over the eastern CONUS and Atlantic Ocean in the entrance of the major vortex jet (Figure 17d), in the entrance region of the minor vortex jet at 120–140°E and 40–60°N and in the core of the minor vortex jet at 140–170°E and 60–80°N (Figure 17g), and in the exit region of the major vortex jet (Figure 17j).

We now take into account the sensitivity of AIRS in observing the temperature perturbations T' of GWs with horizontal/vertical wavelengths of λ_H and λ_z, respectively. Ern et al. (2017) found that for medium-scale GWs with $\lambda_H \leq 600$ km and $\lambda_z \geq 20$ km, the AIRS sensitivity function for T' is $\geq$0.7 (their Figure S3 in Supporting Information S1). Here, the sensitivity function specifies the percentage of the actual GW temperature perturbation, denoted T'_{GW}, that AIRS can observe; for example, a sensitivity function of 100% denotes that the AIRS T' equals T'_{GW}, while 50% denotes that the AIRS T' is only $0.5T'_{GW}$. We assume that if AIRS were to "observe" the HIAMCM GWs, that it would mainly observe those GWs having an AIRS sensitivity function of $\geq$70%. We apply the following AIRS observational filter to the HIAMCM data. We first remove the HIAMCM GWs with $|\lambda_z| < 20$ km via Fourier filtering. We then interpolate T' onto an equally spaced horizontal grid using the formalism from Appendix B of Vadas and Becker (2018), remove GWs with $\lambda_H > 600$ km via Fourier filtering, then interpolate back to the longitude/latitude grid. The results are shown in the middle column of Figure 17. Primary GWs from the core of the major jet and orographic forcing (Figure 17b), the entrance region of the major jet (Figure 17e), the entrance/core regions of the minor jet (Figure 17h), and the exit region of the major jet (Figure 17k) are seen.

The right column in Figure 17 shows the AIRS T' at the same altitudes and times. Comparing with the middle column, good agreement is seen between the horizontal wavelengths, structure, and amplitudes of the observationally filtered HIAMCM GWs and the observed GWs, especially the first two rows. Some differences exist, for example, for the high-latitude GWs generated in the core of the minor vortex jet at 140–160°E and 65–75°N. These GWs are seen in the HIAMCM results (Figure 17g) and in the AIRS data (Figure 17i) but have very small amplitudes in the observationally filtered HIAMCM results (Figure 17h). This discrepancy likely occurs because the simulated background wind (which equals the MERRA-2 wind at this altitude) is different from the actual background wind, such that these HIAMCM GWs have $|\lambda_z| < 20$ km and are therefore nearly entirely removed after applying the observational filter to the HIAMCM results in Figure 17g. Such a discrepancy between the MERRA-2 and actual winds at $z \sim 40$ km likely occurs in regions where meteorology balloon wind measurements (incorporated into the MERRA-2 reanalysis) are relatively scarce, such as likely occurs in northern Asia. Thus the simulated (and observationally filtered) GWs are only as good as the background reanalysis used to nudge the HIAMCM.

4.2. Comparison of VIIRS/DNB GWs With the Simulated GWs in the MLT

We now compare the simulated GWs with those observed by the nadir-viewing Visible Infrared Imaging Radiometer Suite (VIIRS) Day/Night Band (DNB) sensor onboard the Suomi NPP, which is operated by the National Oceanic and Atmospheric Administration (NOAA). Suomi NPP was launched on 28 October 2011, and flies at $z = 834$ km in a sun-synchronous polar orbit. The DNB radiometer was designed for detection of very faint nocturnal signals, for example, lunar reflectance of clouds and the surface, with a 505–890 nm band pass (Miller et al., 2013). The images contain a 3,000 km swath width with global coverage. These observations are dominated by the OH airglow from excited hydroxyl (Miller et al., 2012), which peaks near $z \sim 87$ km and has a vertical full width at half maximum of ~8 km (e.g., Sheese et al., 2014). These observations have been utilized to study small to medium-scale GWs worldwide (Miller et al., 2015), including GWs from deep convection (Azeem et al., 2015;

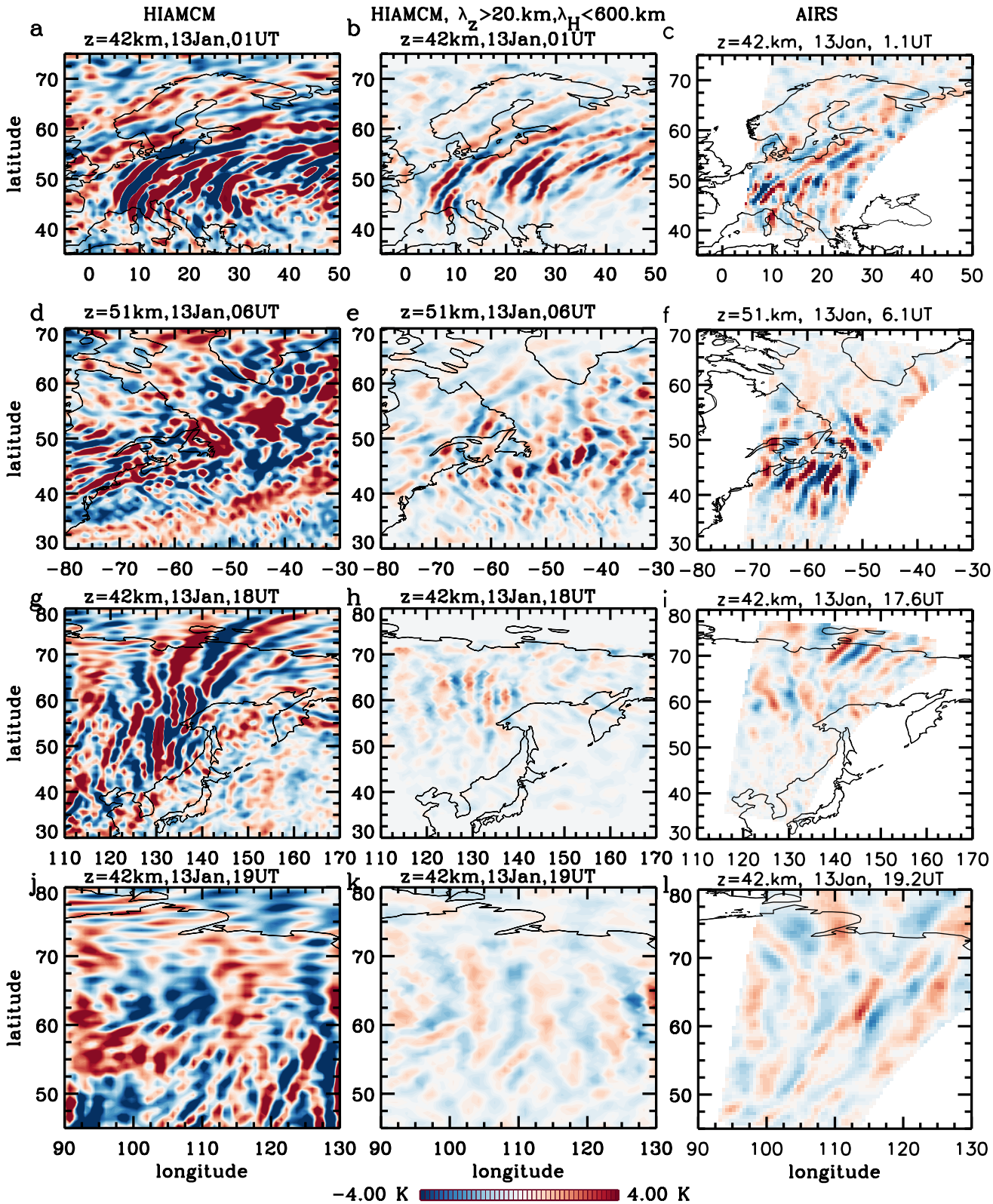

Figure 17. HIAMCM T' (colors, in K) on 13 January 2016 (a, b): 1 UT at $z = 42$ km. (d, e): 6 UT at $z = 51$ km. (g, h): 18 UT at $z = 42$ km. (j, k): 19 UT at $z = 42$ km. The left column shows T' from the HIAMCM. The middle column is the same as the left column except observationally filtered to remove GWs with $|\lambda_z| < 20$ km and $\lambda_H < 600$ km. The right column shows T' observed by AIRS at 1.1 UT (c), 6.1 UT (f), 17.6 UT (i), and 19.2 UT (l). The colors are oversaturated in column 1 to better see the GWs in columns 2 and 3.

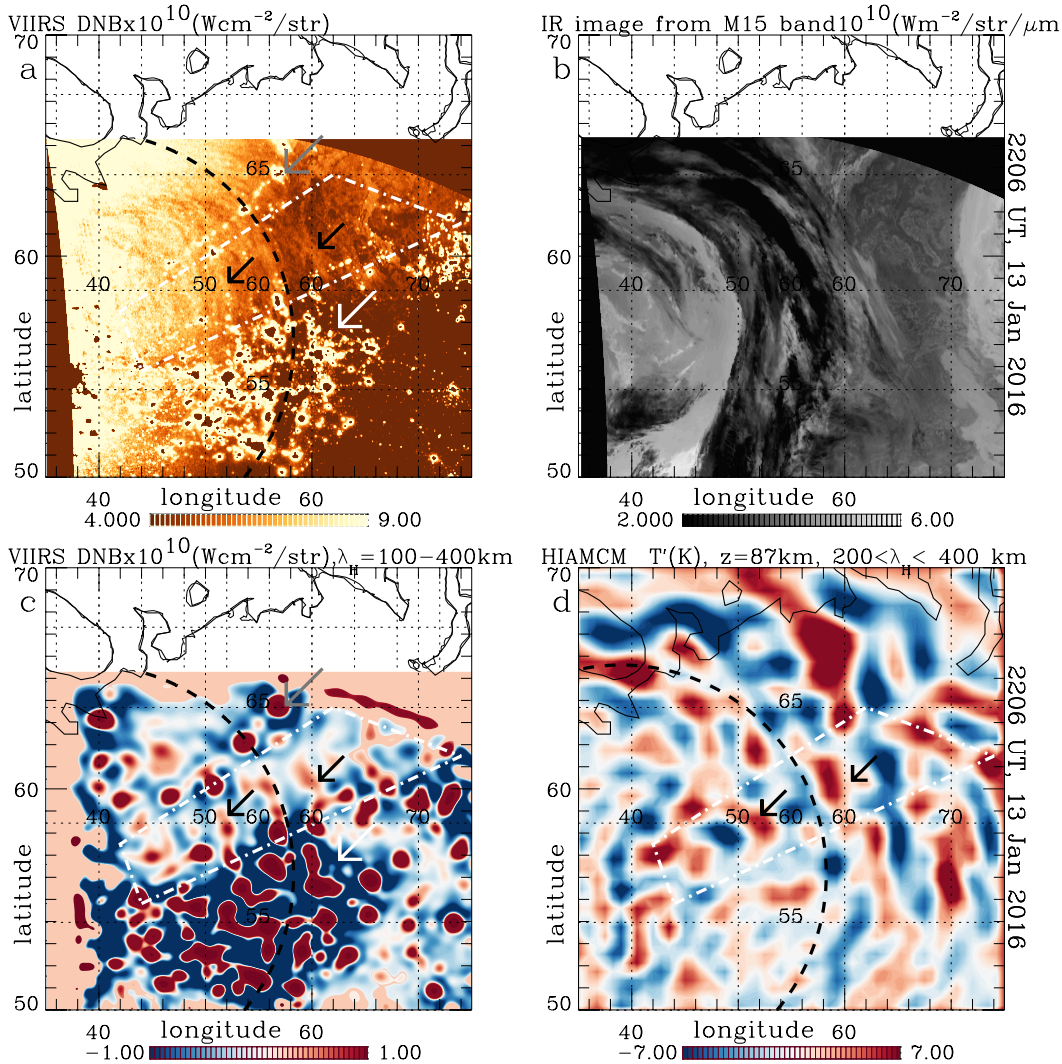

Figure 18. (a) VIIRS/DNB ($\times 10^{10}$ (in Watts/cm^2/steradian)) at 22:06 UT on 13 January 2016 over western Russia. (b) Same as (a), but the IR map from the M15 band showing tropospheric clouds (in Watts/m^2/steradian/μm). (c) Same as (a), but filtered to retain GWs with $100 < \lambda_H < 400$ km. (d) T' from the HIAMCM with $200 < \lambda_H < 400$ km. Here we apply a weighted Gaussian to T' with a full width-half max of 8 km at $z = 87$ km. We then apply a 400 km × 400 km running mean to the image and subtract it from the image to remove GWs with $\lambda_H > 400$ km. Black arrows show small and medium-scale GWs visible by VIIRS/DNB, white (gray) arrows show a large (small) region contaminated by city lights. The white dash-dot trapezoid in (a), (c and d) shows the region with relatively low contamination from city lights. The dashed line shows equi-distances of 1,200 km from 39°E and 56°N. All arrows and dash lines (when shown) appear at the same location in each panel. The colors are oversaturated in (c) to better see the arc-like GWs.

Lai et al., 2017; Miller et al., 2018; Xu et al., 2019; Yue et al., 2014, 2019). Because of contamination from city lights, only GWs over clouds, unpopulated areas and the ocean are visible in VIIRS/DNB. Because VIIRS/DNB is also sensitive to clouds, we use the M15 band IR image, which detect clouds, to determine which waves in the VIIRS/DNB are GWs.

Figures 18a and 18b shows the VIIRS/DNB visible and M15 band IR images, respectively, at 22:06 UT on 13 January 2016 over western Russia at 35–75°E and 50–70°N. White (gray) arrows show a large (small) region contaminated by city lights. The white dash-dot trapezoid in Figure 18a shows the region where the data has relatively low contamination from city lights. Small and medium-scale GWs with arc-like ring structures are seen in the VIIRS/DNB image in Figure 18a. The black arrows point to the visible medium-scale arc-like GWs. We estimate a possible center for these medium-scale GWs by fitting a circle to the phase lines "visually." A dash line shows equi-distances of 1,200 km from 39°E and 56°N. Interestingly, this inferred ring center of 39°E and 56°N is

quite close to the location of the event #1 LBF, 35°E and 60°N, which was the source of the event #1 secondary GWs identified in V23 (see Section 3.1). Figure 18c shows the same VIIRS/DNB observations as in Figure 18a, but filtered to retain GWs with $100 < \lambda_H < 400$ km. The medium-scale GWs with arc-like structures are indicated with black arrows, and are located within the white dash-dot trapezoid. Note that these arrows and the black dash lines are the same as in Figure 18a.

We apply a weighted Gaussian to the HIAMCM T' with a full width-half maximum of 8 km at $z = 87$ km. We then apply a 400 km × 400 km running mean to the image and subtract this from the image to remove GWs with $\lambda_H > 400$ km. Figure 18d shows the result. A complex mix of concentric and arc-like GWs are seen that are centered on eastern Europe. The black arrows, black dash line and white dash-dot trapezoid are in the same locations as in Figures 18a and 18c. Good agreement between the horizontal wavelengths and inferred ring centers of the simulated and observed GWs is seen within the region of relatively low city light contamination (white dash-dot trapezoids). Note that the simulated GWs in Figure 18d are secondary GWs from the dissipation of primary GWs generated/amplified by the core of the major polar vortex jet.

4.3. Comparison of Meteor Radar Wind With the Simulated Wind

We now compare the hourly simulated horizontal wind in the MLT with the horizontal wind measured by the meteor radar in Andenes, Norway and Collm, Germany at $z \sim 80 - 100$ km (Jacobi et al., 2007; Stober et al., 2012) during this 4-day period. The method used to determine these winds are detailed in Stober et al. (2017). This is a very stringent test of model fidelity since most studies that compare models with meteor radar winds use model climatology data which average significantly (e.g., weeks or months) over space and/or time (e.g., Hindley et al., 2022).

Figures 19a and 19b shows keograms of the zonal wind u and meridional wind v measured by the meteor radar at Andenes, Norway (13.0°E, 69.1°N). The largest visible wave is the semi-diurnal tide, as expected. Figure 19k shows the corresponding spectral power, $|\tilde{u}|^2$ and $|\tilde{v}|^2$, averaged from $z = 78 - 98$ km for u and v from Figures 19a and 19b, where $\tilde{u}$ and $\tilde{v}$ are the 2D Fourier transforms of u and v, respectively, at a given z. GWs with periods of $\tau_r \sim 2 - 11$ hr are seen, with the power increasing rapidly with wave period. Figures 19e and 19f show u' and v' for a subset of the GWs, that is, those having $\tau_r < 7$ hr (obtained via Fourier filtering), and Figures 19i and 19j show blow-ups of the GWs from Figures 19e and 19f during 12.5–14.5 January. GWs with $\tau_r \sim 3 - 7$ hr are seen having downgoing and upgoing phases in time.

Figures 19c and 19d shows the HIAMCM u and v at Andenes and Figure 19n shows the corresponding spectral power averaged from $z = 78 - 98$ km. Here, we apply a 600 km × 600 km horizontal running mean smoothing to u and v (which is the approximate field-of-view (FOV) of the meteor radar) in order to better-compare the simulated wind with the observations. Similar to the radar measurements, the semi-diurnal tide has the largest amplitude in Figures 19c and 19d. The simulated GWs in Figure 19n have $\tau_r \sim 2 - 11$ hr with a similar spectral shape as for the observed GWs in Figure 19k. Figures 19g and 19h show the simulated GWs with $\tau_r < 7$ hr, and Figures 19l and 19m show blow-ups of the GWs from Figures 19g and 19h during 12.5–14.5 January. These GWs have downward and upward phases in time, similar to the meteor radar observations. In general, the simulated GWs have similar characteristics (τ_r and λ_z) as the observed GWs. Since the simulated upward and downward-propagating GWs in the MLT are secondary and higher-order GWs generated/amplified by (i.e., from) the polar vortex jet, Figure 19 strongly suggests that the meteor radar observed upward and downward-propagating secondary and higher-order GWs from the polar vortex jet.

In general, the amplitudes of the simulated GWs and simulated semi-diurnal tide are somewhat larger than the observed values in Figure 19. This can occur for several reasons. First, the 600 km × 600 km running mean smoothing we applied to the HIAMCM winds do not duplicate the complicated process used to obtain the meteor radar winds (see Stober et al., 2017). Second, the GW-tidal interactions resolved by the HIAMCM may differ from the real atmosphere, thereby causing somewhat too strong tidal and GW wind amplitudes. (For discussions of GW-tidal interactions, see Senf and Achatz (2011), Becker (2017), Becker and Oberheide (2023).)

The corresponding results at Collm, Germany (13.0°E, 51.3°N) are shown in Figure 20. The spectra of the observed and simulated GWs are similar. Additionally the observed and simulated GWs have downward and upward phase lines in time, indicating the likely presence of upward and downward-propagating GWs,

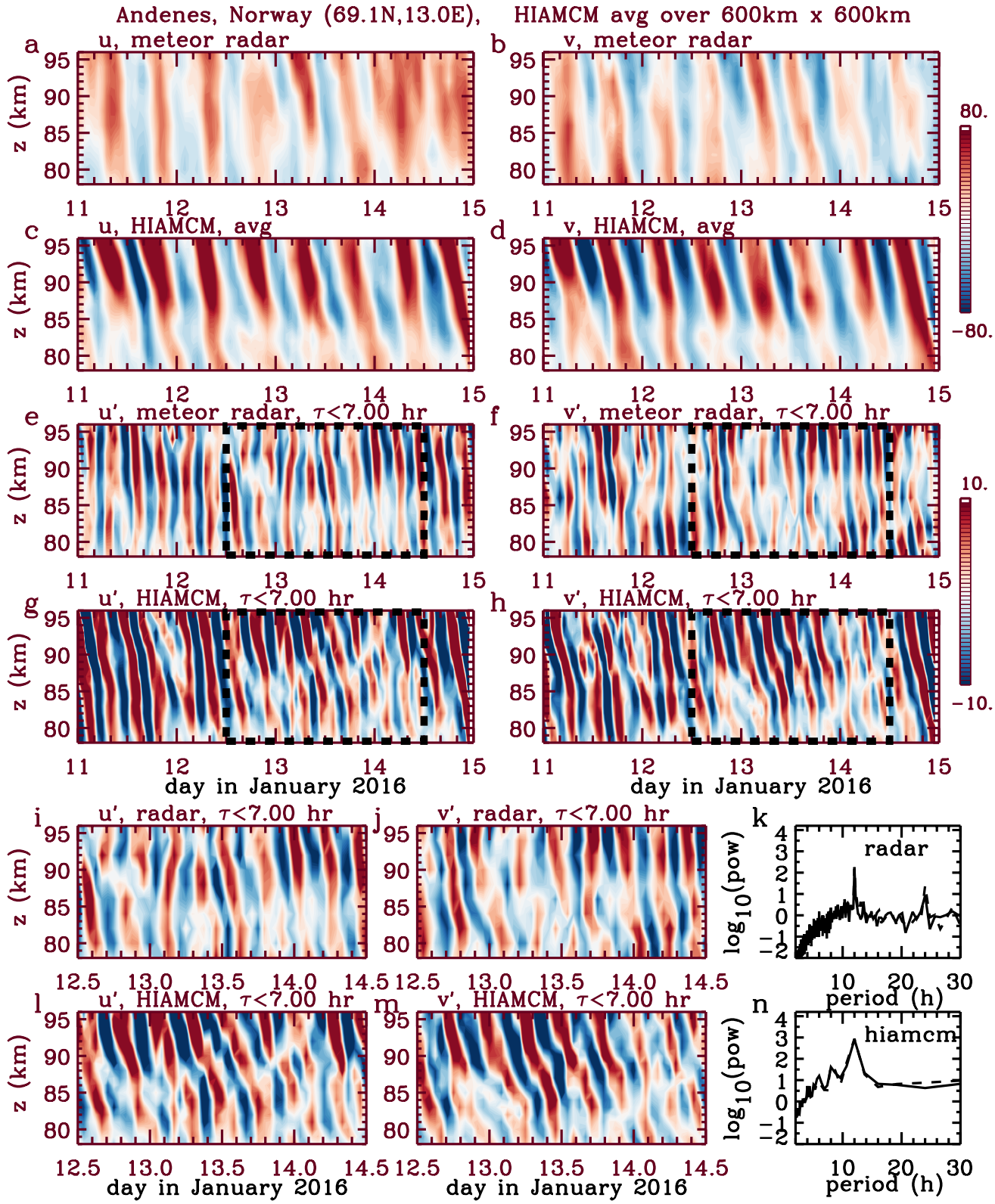

Figure 19.

respectively. Note the lack of the diurnal tide in the model results (compare Figures 19n and 20n), although this tide has a significantly smaller amplitude than that of the semi-diurnal tide (see Figures 19k and 20k).

5. Conclusions and Discussion

In this paper, we modeled the GWs during 11–14 January 2016 from the ground to the thermosphere with the HIAMCM. Since no geomagnetic forcing was included, all simulated GWs were generated by multi-step vertical coupling (MSVC) of the primary GW sources in the troposphere and stratosphere. We found that the entrance, core and exit regions of the polar vortex jet generated primary GWs in the stratosphere and that these generation regions could be identified from MKS formalism. We found that in general, these primary GWs and those from the troposphere broke/dissipated at $z \sim 70-80$ km or farther below, whereby the atmosphere generated upward and downward-propagating secondary GWs in response. Since most of the secondary GWs had large periods and therefore small ascent angles to the horizontal, they propagated large distances horizontally. Upon reaching the MLT, these GWs spanned a large latitudinal range of 20–90°N. These secondary GWs broke/dissipated at $z \sim 100-110$ km, whereby the atmosphere generated upward and downward-propagating medium to large-scale higher-order GWs. In the mid thermosphere, higher-order medium-scale GWs with concentric ring and arc-like structures were prevalent over the entrance, core and exit regions of the major and minor polar vortex jet cores. These higher-order GWs spanned $10-90$°N. Those with the largest amplitudes generally propagated against the background wind.

We found that many medium to large-scale higher-order GWs generated over Europe and Asia propagated over the Arctic region then southward over the CONUS to $\sim 15-20$°N daily at $\sim 14-24$ UT ($\sim 9-16$ LT) due to the favorable northward background wind component over the CONUS during that time. Such GWs could be accidently "misidentified" as being generated by auroral activity because of their southward propagation direction over the CONUS around LT noon, their horizontal wavelengths, and their apparent source location in the Arctic region.

We also found that large-scale GWs with $T' \sim 20-40$ K, $\lambda_H \sim 3{,}000$ km, $c_H \sim 650$ m/s and $\tau_r \sim 1.3$ hr were generated at mid to high latitudes at $z \sim 100-110$ km. These GWs propagated southwestward at $z = 200$ km at ~8–16 LT where the background wind (mainly from the diurnal tide) was northeastward. These GWs may have been generated by the LBFs created by the dissipation of secondary GWs from below. These LBFs exhibited semidiurnal variability due to the strong semi-diurnal tides in the MLT. These large-scale GWs may be related to the large-scale wintertime GWs observed by ICON-MIGHTI (Cullens et al., 2022; Triplett et al., 2023). Indeed, Cullens et al. (2022) found that the monthly zonal-mean perturbations in the zonal wind at $z = 200$ km peaked at June–July and December–January, with the December–January GW peak increasing with increasing latitude in the northern hemisphere winter.

We also found that the mean potential energy density PE increased up to $z \sim 70$ km, decreased at $z \sim 70$–80 km where the primary GWs dissipated, increased at $z \sim 80$–110 km from the secondary GWs, and then decreased at $z \sim 110$ km where the secondary GWs dissipated. The PE then decreased at $z = 110$–350 km. These model results are similar to observations, which found an increase of the PE in the stratosphere and lower mesosphere, then a decrease in the mesosphere (Chu et al., 2022; Liu et al., 2019; Lu et al., 2015). Additionally, Chu et al. (2022) recently found a second peak in the PE at $z \simeq 113$ km, with a decrease in the PE at $z > 113$ km (their Figure 3a), similar to our model result. However, because their Figure 3a does not extend above $z > 115$ km, we cannot verify if the PE continues to decrease at $z > 115$ km. Future measurements to higher altitudes are necessary to confirm this model result.

Finally, we compared our model results with multiple observations. We found good agreement of the horizontal wavelengths, structure, and amplitudes between the simulated primary GWs from the entrance, core and exit regions of the polar vortex jet with those observed by AIRS. We also found good agreement between the simulated secondary GWs with those observed by the Rayleigh lidar at ALOMAR. We observed concentric GWs

Figure 19. Keograms of u (a) and v (b) measured by the meteor radar at Andenes, Norway (13.0°E, 69.1°N) during 11–15 January 2016 (colors, in m/s). Keograms of u (c) and v (d) from the HIAMCM averaged horizontally over 600 km × 600 km at Andenes. Keograms of u' (e) and v' (f) for observed GWs with $\tau_r < 7$ hr from (a) and (b). Keograms of u' (g) and v' (h) for HIAMCM GWs with $\tau_r < 7$ hr from (c) and (d). (i, j, l, m): Blow-ups of the GWs in the black dash boxes in (e–h), respectively, during 12.5–14.5 January. (k): Logarithm of the spectral power $|\tilde{u}|^2$ (solid line) and $|\tilde{v}|^2$ (dash line) averaged from $z = 78-98$ km for observed u and v from (a and b). (n): Same as (k) but for HIAMCM u and v from (c and d).

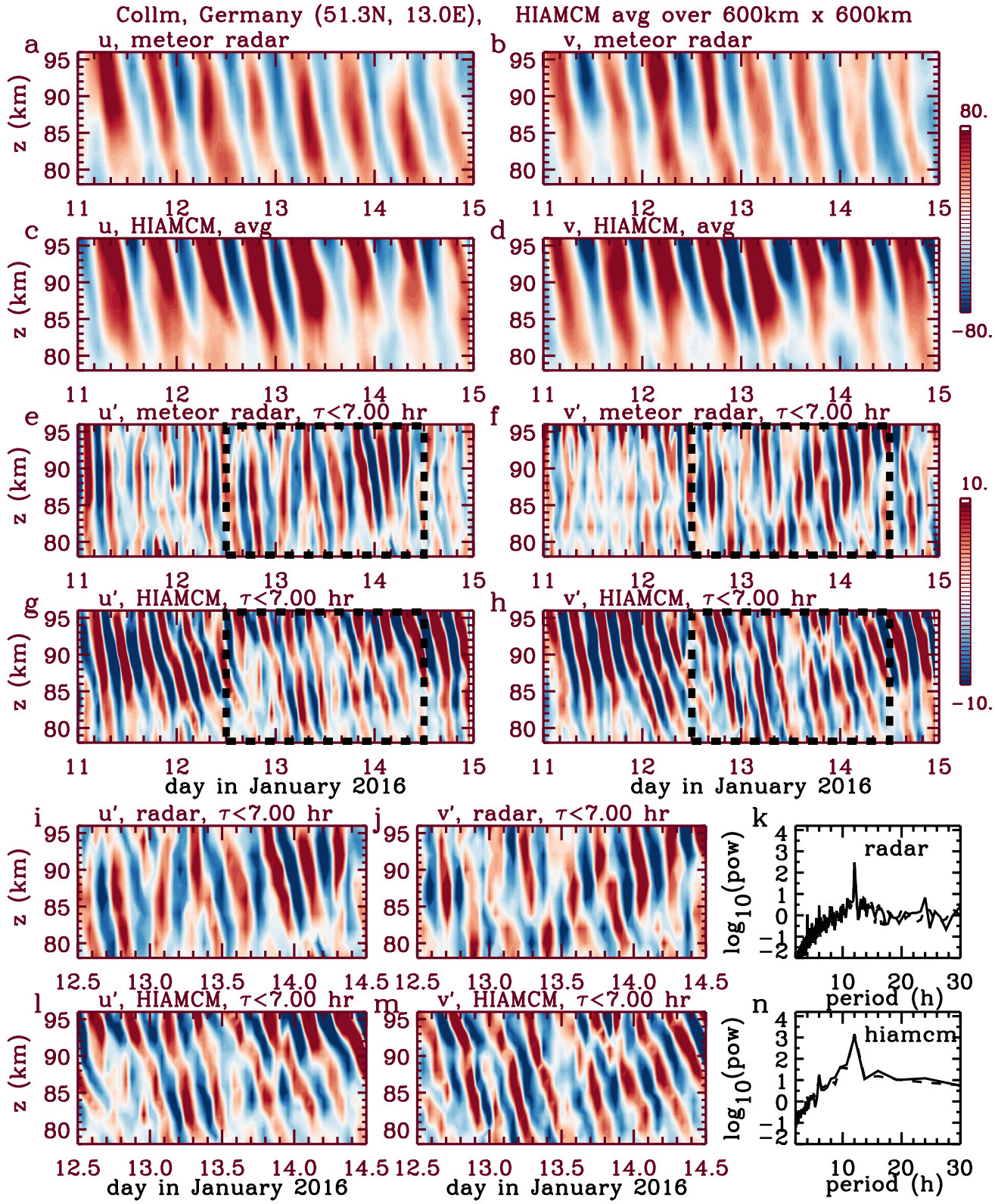

Figure 20. Same as Figure 19 but at Collm, Germany (13.0°E, 51.3°N).

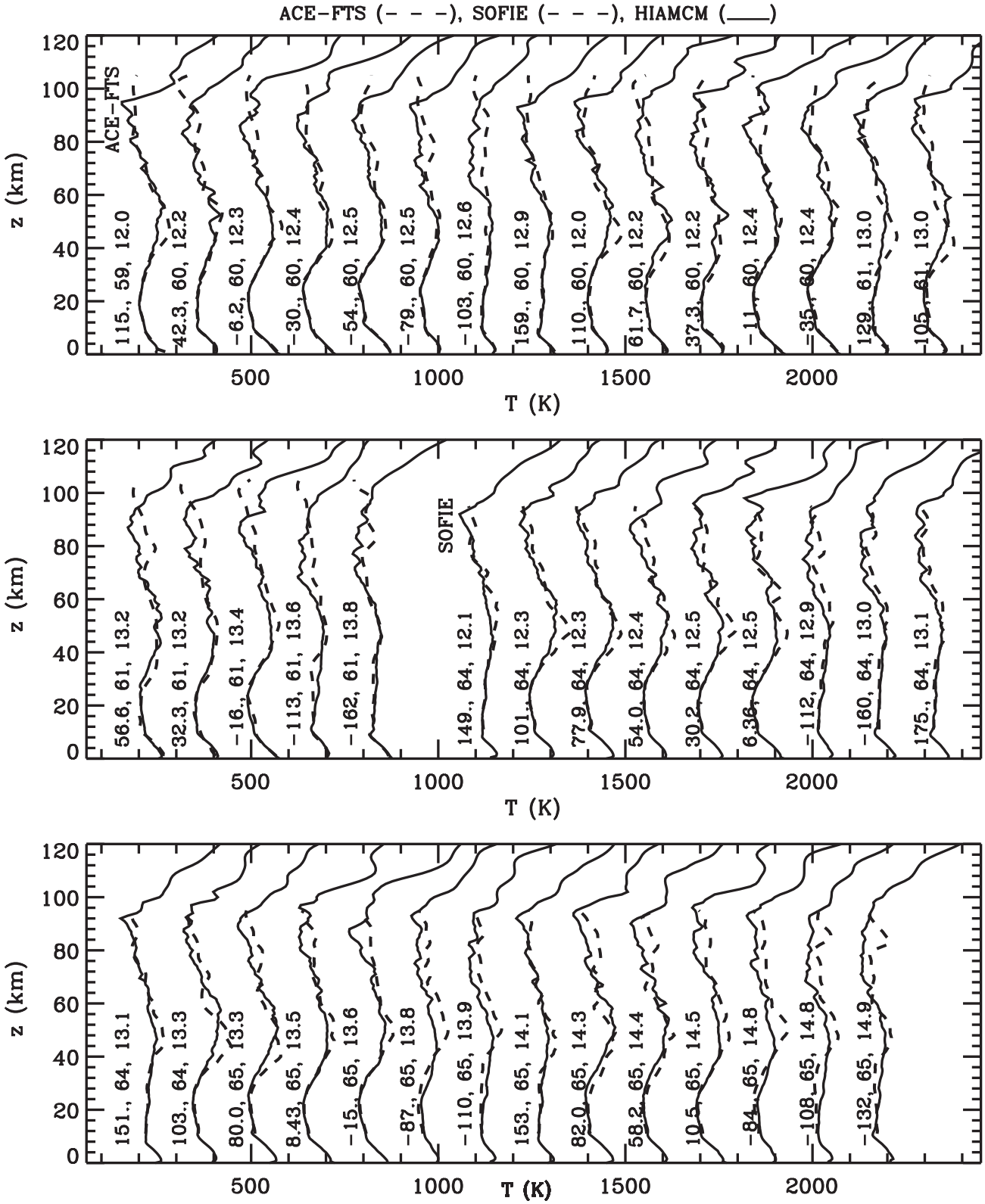

Figure 21. ACE-FTS temperature (dashed lines, first row and first five profiles from second row) and SOFIE temperature (dashed lines, all but first five profiles in second row and all of third row). The HIAMCM temperatures are shown as solid lines. Each profile is labeled with the longitude (in degrees E), latitude (in degrees N) and daynumber. Each profile is shifted to the right for clarity, with a double shift occurring between the ACE-FTS and SOPHIE profiles in the second row.

over eastern Europe from VIIRS/DNB observations with an inferred center at 39°E and 56°N. For the scales resolvable by the HIAMCM and within the region with relatively low contamination from city lights, we found good agreement between the horizontal wavelengths and inferred ring centers of the simulated and observed GWs. Finally, we found reasonable agreement between the simulated winds in the MLT with those observed by meteor radars in Europe. In particular, we showed that the meteor radar likely observed upward and downward-propagating secondary and higher-order GWs from the polar vortex jet. We conclude that the polar vortex jet is an important source of primary GWs, giving rise to higher-order GWs with medium to large horizontal scales in the northern winter thermosphere via MSVC.

Appendix A: Comparison of ACE-FTS, SOFIE and Model Temperatures

In this appendix, we compare the model temperatures with those measured by the Atmospheric Chemistry Experiment Fourier Transform Spectrometer (ACE-FTS) (Bernath et al., 2005) and Solar Occultation For Ice Experiment (SOFIE) (Gordley et al., 2009; Russell et al., 2009). We utilize ACE-FTS version 4.1 and SOFIE version 1.3 data, which have vertical resolutions in the mesosphere of $2-2.5$ km (Boone et al., 2020) and 1.6 km (Marshall et al., 2011), respectively. ACE-FTS retrieves temperature from $z = 18-125$ km (García-Comas et al., 2014; Sica et al., 2008). SOFIE retrieves temperature from $z = 15-102$ km (Hervig et al., 2016). We show ACE-FTS temperatures below 105 km, and SOFIE temperatures below 95 km. Figure 21 shows the ACE-FTS temperature (dashed lines, first row and first five profiles from second row) and SOFIE temperature (dashed lines, all but first five profiles in the second row and all of third row). The HIAMCM temperatures are shown as solid lines. Each profile is labeled with longitude (in degrees E), latitude (in degrees N) and daynumber. We see reasonable agreement between the simulated and SOFIE temperatures. The ACE-FTS temperatures agree less well with the simulated temperatures at $z > 70$ km.

Data Availability Statement

MERRA-2 reanalysis data is available in English for download at https://gmao.gsfc.nasa.gov/reanalysis/MERRA-2/data_access/. VIIRS/DNB and M15 data are available at https://ladsweb.modaps.eosdis.nasa.gov/archive/allData/5200/. AIRS full-resolution temperature retrieval data are accessible at https://datapub.fz-juelich.de/slcs/airs/gravity_waves. ACE-FTS is onboard SCISAT, and is a Canadian-led mission mainly supported by the Canadian Space Agency. ACE-FTS data are available at https://earth.esa.int/eogateway/catalog/scisat-1-ace-fts-and-maestro. SOFIE data are available at https://sofie.gats-inc.com/. The model data shown in this paper will be available at the time of publication at https://www.cora.nwra.com/vadas/Vadas-etal-JGR-2024-polarvortex-thermosphere-files/.

Acknowledgments
SLV was supported by NSF Grants AGS-1832988 and 2329957. SLV and EB were supported by NASA Grants 80NSSC20K0628, 80NSSC19K0836, 80NSSC22K0174, and 80NSSC24K0274. KB was supported by NSF Grant AGS-2052993 and NASA Grants 80NSSC19K0836 and 80NSSC21K0002. YH is funded by NASA Heliophysics Living With a Star Tools 80NSSC22K0641 and ONR RAM-HORN. Gunter Stober is a member of the Oeschger Center for Climate Change Research (OCCR). VLH acknowledges support from NASA Grants 80NSSC22K0017 and 80NSSC23K0848. GB acknowledges the support by the project W1 (Gravity wave parameterizations for the atmosphere) of the Collaborative Research Centre TRR 181 "Energy Transfers in Atmosphere and Ocean" funded by the Deutsche Forschungsgemeinschaft (DFG, German Research Foundation) under project number 274762653. LH acknowledges the Juelich Supercomputing Centre for providing computing time on the JUWELS cluster to process the AIRS high-resolution temperature retrievals.

References

Achatz, U. (2007). Gravity-wave breaking: Linear and primary nonlinear dynamics. *Advances in Space Research*, *40*(6), 719–733. https://doi.org/10.1016/j.asr.2007.03.078

Achatz, U. (2022). *Atmospheric dynamics* (p. 554). Springer-Verlag GmbH Germany, part of Springer Nature. https://doi.org/10.1007/978-3-662-63941-2

Alexander, M. J., & Teitelbaum, H. (2011). Three-dimensional properties of Andes mountain waves observed by satellite: A case study. *Journal of Geophysical Research*, *116*, D23110. https://doi.org/10.1029/2011JD016151

Avsarkisov, V., Becker, E., & Renkwitz, T. (2022). Turbulent parameters in the middle atmosphere: Theoretical estimates deduced from a gravity wave–resolving general circulation model. *Journal of the Atmospheric Sciences*, *79*(4), 933–952. https://doi.org/10.1175/JAS-D-21-0005.1

Azeem, I., Yue, J., Hoffmann, L., Miller, S. D., Straka, W. C., III., & Crowley, G. (2015). Multisensor profiling of a concentric gravity wave event propagating from the troposphere to the ionosphere. *Geophysical Research Letters*, *42*(19), 7874–7880. https://doi.org/10.1002/2015GL065903

Becker, E. (2017). Mean-flow effects of thermal tides in the mesosphere and lower thermosphere. *Journal of the Atmospheric Sciences*, *74*(6), 2043–2063. https://doi.org/10.1175/JAS-D-16-0194.1

Becker, E., Goncharenko, L., Harvey, V. L., & Vadas, S. L. (2022). Multi-step vertical coupling during the January 2017 sudden stratospheric warming. *Journal of Geophysical Research: Space Physics*, *127*(12), e2022JA030866. https://doi.org/10.1029/2022JA030866

Becker, E., & Oberheide, J. (2023). Unexpected DE3 tide in the southern summer mesosphere. *Geophysical Research Letters*, *50*(20), e2023GL104368. https://doi.org/10.1029/2023GL104368

Becker, E., & Vadas, S. L. (2018). Secondary gravity waves in the winter mesosphere: Results from a high-resolution global circulation model. *Journal of Geophysical Research: Atmospheres*, *123*(5), 2605–2627. https://doi.org/10.1002/2017JD027460

Becker, E., & Vadas, S. L. (2020). Explicit global simulation of gravity waves in the thermosphere. *Journal of Geophysical Research: Space Physics*, *125*(10), e2020JA028034. https://doi.org/10.1029/2020JA028034

Becker, E., Vadas, S. L., Bossert, K., Harvey, V. L., Zülicke, C., & Hoffmann, L. (2022). A high-resolution whole-atmosphere model with resolved gravity waves and specified large-scale dynamics in the troposphere and stratosphere. *Journal of Geophysical Research: Space Physics*, *127*(2), e2021JD035018. https://doi.org/10.1029/2021JD035018

Bernath, P. F., McElroy, T., Abrams, M. C., Boone, C. D., Butler, C. C. M., Carleer, M., et al. (2005). Atmospheric chemistry experiment (ACE): Mission overview. *Geophysical Research Letters*, *32*(L15S01). https://doi.org/10.1029/2005GL022386

Boone, C., Bernath, P., Cok, D., Jones, S., & Steffen, J. (2020). Version 4 retrievals for the atmospheric chemistry experiment fourier transform spectrometer (ACE-FTS) and imagers. *Journal of Quantitative Spectroscopy & Radiative Transfer*, *247*, 106939. https://doi.org/10.1016/j.jqsrt.2020.106939

Bossert, K., Fritts, D. C., Williams, B. P., Kruse, C. G., Heale, C. J., Pautet, P.-D., et al. (2017). Secondary gravity wave generation over New Zealand during the DEEPWAVE campaign. *Journal of Geophysical Research: Atmospheres*, *122*(15), 7834–7850. https://doi.org/10.1002/2016JD026079

Bossert, K., Vadas, S. L., Hoffmann, L., Becker, E., Harvey, V. L., & Bramberger, M. (2020). Observations of stratospheric gravity waves over Europe on 12 January 2016: The role of the polar night jet during the DEEPWAVE campaign. *Journal of Geophysical Research: Atmospheres*, *125*(21), e2020JD032893. https://doi.org/10.1029/2020JD032893

Chen, C., Chu, X., McDonald, A. J., Vadas, S. L., Yu, Z., Fong, W., & Lu, X. (2013). Inertia-gravity waves in Antarctica: A case study using simultaneous lidar and radar measurements at McMurdo/Scott Base (77.8°S, 166.7°E). *Journal of Geophysical Research: Atmospheres*, *118*(7), 2794–2808. https://doi.org/10.1002/jgrd.50318

Chu, X., Gardner, C., Li, X., & Lin, C.-T. (2022). Vertical transport of sensible heat and meteoric Na by the complete temporal spectrum of gravity waves in the MLT above McMurdo (77.84°S, 166.67°E), Antarctica. *Journal of Geophysical Research: Atmospheres*, *127*(16), e2021JD035728. https://doi.org/10.1029/2021JD035728

Chun, H.-Y., & Kim, Y.-H. (2008). Secondary waves generated by breaking of convective gravity waves in the mesosphere and their influence in the wave momentum flux. *Journal of Geophysical Research*, *113*, D23107. https://doi.org/10.1029/2008JD009792

Crowley, G., Jones, T. B., & Dudeney, J. R. (1987). Comparison of short period TID morphologies in Antarctica during geomagnetically quiet and active intervals. *Journal of Atmospheric and Terrestrial Physics*, *49*(11), 1155–1162. https://doi.org/10.1016/0021-9169(87)90098-5

Crowley, G., & Rodrigues, F. S. (2012). Characteristics of traveling ionospheric disturbances observed by the TIDDBIT sounder. *Radio Science*, *47*(4), RS0L22. https://doi.org/10.1029/2011RS004959

Cullens, C., England, S. L., Immel, T. J., Maute, A., Harding, B. J., Triplett, C. C., et al. (2022). Seasonal variations of medium-scale waves observed by ICON-MIGHTI. *Geophysical Research Letters*, *49*(17), e2022GL099383. https://doi.org/10.1029/2022GL099383

Eckermann, S. D., & Preusse, P. (1999). Global measurements of stratospheric mountain waves from space. *Science*, *286*(5444), 1534–1537. https://doi.org/10.1126/science.286.5444.1534

Eckermann, S. D., Doyle, J. D., Reinecke, P. A., Reynolds, C. A., Smith, R. B., Fritts, D. C., & Dörnbrack, A. (2019). Stratospheric gravity wave products from satellite infrared nadir radiances in the planning, execution, and validation of aircraft measurements during DEEPWAVE. *Journal of Applied Meteorology and Climatology*, *58*(9), 2049–2075. https://doi.org/10.1175/JAMC-D-19-0015.1

Ern, M., Hoffmann, L., & Preusse, P. (2017). Directional gravity wave momentum fluxes in the stratosphere derived from high-resolution AIRS temperature data. *Geophysical Research Letters*, *44*(1), 475–485. https://doi.org/10.1002/2016GL072007

Forbes, J. M. (2007). Dynamics of the thermosphere. *Journal of the Meteorological Society of Japan*, *85B*, 193–213. https://doi.org/10.2151/jmsj.85b.193

Fovell, R., Durran, D., & Holton, J. (1992). Numerical simulation of convectively generated gravity waves. *Journal of the Atmospheric Sciences*, *49*(16), 1427–1442. https://doi.org/10.1175/1520-0469(1992)049<1427:nsocgs>2.0.co;2

Frissell, N. A., Baker, J. B. H., Ruohoniemi, J. M., Greenwald, R. A., Gerrard, A. J., Miller, E. S., & West, M. L. (2016). Sources and characteristics of medium-scale traveling ionospheric disturbances observed by high-frequency radars in the North American sector. *Journal of Geophysical Research: Space Physics*, *121*(4), 3722–3739. https://doi.org/10.1002/2015JA022168

Fritts, D. C., Smith, R., Taylor, M., Doyle, J., Eckermann, S., Dornbrack, A., et al. (2016). The deep propagating gravity wave experiment (DEEPWAVE): An airborne and ground-based exploration of gravity wave propagation and effects from their sources throughout the lower and middle atmosphere. *Bulletin America Meteorology Social*, *97*(3), 425–453. https://doi.org/10.1175/BAMS-D-14-00269.1

Fritts, D. C., & Alexander, M. J. (2003). Gravity wave dynamics and effects in the middle atmosphere. *Reviews of Geophysics*, *41*(1003). https://doi.org/10.1029/2001/RG000106

Fritts, D. C., Lund, T. S., Wan, K., & Liu, H.-L. (2021). Numerical simulation of mountain waves over the Southern Andes. Part II: Momentum fluxes and wave-mean-flow interactions. *Journal of the Atmospheric Sciences*, *78*(10), 3069–3088. https://doi.org/10.1175/JAS-D-20-0207.1

Fritts, D. C., & Vadas, S. L. (2008). Gravity wave penetration into the thermosphere: Sensitivity to solar cycle variations and mean winds. *Annales Geophysicae*, *26*(12), 3841–3861. https://doi.org/10.5194/angeo-26-3841-2008

Fritts, D. C., Vadas, S. L., & Yamada, Y. (2002). An estimate of strong local body forcing and gravity wave radiation based on OH airglow and meteor radar observations. *Geophysical Research Letters*, *29*(10). https://doi.org/10.1029/2001GL013753

Fritts, D. C., Wang, L., & Werne, J. A. (2013). Gravity wave-fine structure interactions. Part I: Influences of fine structure form and orientation on flow evolution and instability. *Journal of the Atmospheric Sciences*, *70*(12), 3710–3734. https://doi.org/10.1175/JAS-D-13-055.1

García-Comas, M., Funke, B., Gardini, A., López-Puertas, M., Jurado-Navarro, A., von Clarmann, T., et al. (2014). MIPAS temperature from the stratosphere to the lower thermosphere: Comparison of VM21 with ACE-FTS, MLS, OSIRIS, SABER, SOFIE and lidar measurements. *Atmospheric Measurement Techniques*, *7*(11), 3633–3651. https://doi.org/10.5194/amt-7-3633-2014

Gelaro, R., McCarty, W., Suárez, M. J., Todling, R., Molod, A., Takacs, L., et al. (2017). The modern-era retrospective analysis for research and applications, version 2 (MERRA-2). *Journal of Climate*, *30*(14), 5419–5454. https://doi.org/10.1175/JCLI-D-16-0758.1

Gong, J., Wu, D., & Eckermann, S. (2012). Gravity wave variances and propagation derived from AIRS radiances. *Atmospheric Chemistry and Physics*, *12*(4), 1701–1720. https://doi.org/10.5194/acp-12-1701-2012

Gordley, L., Hervig, M., Fish, C., Russell, J., Bailey, S., Cook, J., et al. (2009). The solar occultation for ice experiment. *Journal of Atmospheric and Solar-Terrestrial Physics*, *71*(3–4), 300–315. https://doi.org/10.1016/j.jastp.2008.07.012

Harvey, V. L., Randall, C. E., Goncharenko, L. P., Becker, E., Forbes, J. M., Carstens, J., et al. (2023). CIPS observations of gravity wave activity at the edge of the polar vortices and coupling to the ionosphere. *Journal of Geophysical Research: Atmospheres*, *128*(12), e2023JD038827. https://doi.org/10.1029/2023JD038827

Heale, C. J., Inchin, P. A., & Snively, J. B. (2022). Primary versus secondary gravity wave responses at F-region heights generated by a convective source. *Journal of Geophysical Research: Space Physics*, *127*(1), e2021JA029947. https://doi.org/10.1029/2021JA029947

Heale, C. J., Snively, J. B., Bhatt, A. N., Hoffmann, L., Stephan, C. C., & Kendall, E. A. (2019). Multilayer observations and modeling of thunderstorm generated gravity waves over the midwestern United States. *Geophysical Research Letters*, *46*(23), 14164–14174. https://doi.org/10.1029/2019GL085934

Hervig, M. E., Gerding, M., Stevens, M. H., Stockwell, R., Bailey, S. M., Russell, J. M., III., & Stober, G. (2016). Mid-latitude mesospheric clouds and their environment from SOFIE observations. *Journal of Atmospheric and Solar-Terrestrial Physics*, *149*, 1–14. https://doi.org/10.1016/j.jastp.2016.09.004

Hindley, N. P., Mitchell, N. J., Cobbett, N., Smith, A. K., Fritts, D. C., Janches, D., et al. (2022). Radar observations of winds, waves and tides in the mesosphere and lower thermosphere over South Georgia Island (54°S, 36°W) and comparison to WACCM simulations. *Atmospheric Chemistry and Physics*. https://doi.org/10.5194/acp-2021-981

Hindley, N. P., Wright, C. J., Gadian, A. M., Hoffmann, L., Hughes, J. K., Jackson, D. R., et al. (2021). Stratospheric gravity-waves over the mountainous island of South Georgia: Testing a high-resolution dynamical model with 3-D satellite observations and radiosondes. *Atmospheric Chemistry and Physics*, *21*(10), 7695–7722. https://doi.org/10.5194/acp-21-7695-2021

Hines, C. O. (1960). Internal atmospheric gravity waves at ionospheric heights. *Canadian Journal of Physics*, *38*(11), 1441–1481. https://doi.org/10.1139/p60-150

Hoffmann, L., & Alexander, M. (2009). Retrieval of stratospheric temperatures from Atmospheric Infrared Sounder Radiance measurements for gravity wave studies. *Journal of Geophysical Research*, *114*(D7), D07105. https://doi.org/10.1029/2008JD011241

Hoffmann, L., Xue, X., & Alexander, M. J. (2013). A global view of stratospheric gravity wave hotspots located with Atmospheric Infrared Sounder observations [Dataset]. *Journal of Geophysical Research: Atmospheres*, *118*(2), 416–434. https://doi.org/10.1029/2012JD018658

Holt, L. A., Alexander, M. J., Coy, L., Liu, C., Molod, A., Putman, W., & Pawson, S. (2017). An evaluation of gravity waves and gravity wave sources in the southern hemisphere in a 7 km global climate simulation. *Quarterly Journal of the Royal Meteorological Society*, *143*(707), 2481–2495. https://doi.org/10.1002/qj.3101

Holton, J. R., & Alexander, M. J. (1999). Gravity waves in the mesosphere generated by tropospheric convection. *Tellus*, *51A-B*, 45–58. https://doi.org/10.3402/tellusa.v51i1.12305

Holton, J. R. (1983). The influence of gravity wave breaking on the general circulation of the middle atmosphere. *Journal of the Atmospheric Sciences*, *40*(10), 2497–2507. https://doi.org/10.1175/1520-0469(1983)040<2497:tiogwb>2.0.co;2

Horinouchi, T., Nakamura, T., & Kosaka, J.-I. (2002). Convectively generated mesoscale gravity waves simulated throughout the middle atmosphere. *Geophysical Research Letters*, *29*(21), 2007. https://doi.org/10.1029/2002GL016069

Jacobi, C., Fröhlich, K., Viehweg, C., Stober, G., & Kürschner, D. (2007). Midlatitude mesosphere/lower thermosphere meridional winds and temperatures measured with meteor radar. *Advances in Space Research*, *39*(8), 1278–1283. https://doi.org/10.1016/j.asr.2007.01.003

Jiang, J. H., Eckermann, S. D., Wu, D. L., & Ma, J. (2004). A search for mountain waves in MLS stratospheric limb radiances from the winter northern hemisphere: Data analysis and global mountain wave modeling. *Journal of Geophysical Research*, *109*(D3), D03–D107. https://doi.org/10.1029/2003JD003974

Kogure, M., Yue, J., Nakamura, T., Hoffmann, L., Vadas, S., Tomikawa, Y., et al. (2020). First direct observational evidence for secondary gravity waves generated by mountain waves over the Andes. *Geophysical Research Letters*, *47*(17). https://doi.org/10.1029/2020GL088845

Lai, C., Yue, J., Xu, J., Straka, W., Miller, S. D., & Liu, X. (2017). Suomi NPP VIIRS/DNB imagery of nightglow gravity waves from various sources over China. *Advances in Space Research*, *59*(8), 1951–1961. https://doi.org/10.1016/j.asr.2017.01.041

Lane, T. P., Reeder, M. J., & Clark, T. L. (2001). Numerical modeling of gravity waves generated by deep tropical convection. *Journal of the Atmospheric Sciences*, *58*(10), 1249–1274. https://doi.org/10.1175/1520-0469(2001)058<1249:nmogwg>2.0.co;2

Li, F., Liu, A. Z., Swenson, G. R., Hecht, J. H., & Robinson, W. A. (2005). Observations of gravity wave breakdown into ripples associated with dynamical instabilities. *Journal of Geophysical Research*, *110*(D09S11), D09S11. https://doi.org/10.1029/2004JD004849

Lighthill, J. (1978). *Waves in fluids* (p. 504). Cambridge University Press.

Lindzen, R. S. (1981). Turbulence and stress owing to gravity wave and tidal breakdown. *Journal of Geophysical Research*, *86*(C10), 9707–9714. https://doi.org/10.1029/jc086ic10p09707

Liu, X., Xu, J., Yue, J., Vadas, S. L., & Becker, E. (2019). Orographic primary and secondary gravity waves in the middle atmosphere from 16-year SABER observations. *Geophysical Research Letters*, *46*(8), 4512–4522. https://doi.org/10.1029/2019GL082256

Lu, X., Chu, X., Fong, W., Chen, C., Yu, Z., Roberts, B. R., & McDonald, A. J. (2015). Vertical evolution of potential energy density and vertical wave number spectrum of Antarctic gravity waves from 35 to 105 km at McMurdo (77.8°S, 166.7°E). *Journal of Geophysical Research: Atmospheres*, *120*(7), 2719–2737. https://doi.org/10.1002/2014JD022751

Lund, T. S., & Fritts, D. C. (2012). Numerical simulation of gravity wave breaking in the lower thermosphere. *Journal of Geophysical Research*, *117*(D21105), D21105. https://doi.org/10.1029/2012JD017536

Lund, T. S., Fritts, D. C., Wan, K., Laughman, B., & Liu, H.-L. (2020). Numerical simulation of mountain waves over the Southern Andes. Part I: Mountain wave and secondary wave character, evolutions, and breaking. *Journal of the Atmospheric Sciences*, *77*(12), 4337–4356. https://doi.org/10.1175/JAS-D-19-0356.1

Marshall, B. T., Deaver, L. E., Thompson, R. E., Gordley, L. L., McHugh, M. J., Hervig, M. E., & Russell, J. M., III. (2011). Retrieval of temperature and pressure using broadband solar occultation: SOFIE approach and results. *Atmospheric Measurement Techniques*, *4*(5), 893–907. https://doi.org/10.5194/amt-4-893-2011

Matthias, V., Dörnbrack, A., & Stober, G. (2016). The extraordinarily strong and cold polar vortex in the early northern winter 2015/2016. *Geophysical Research Letters*, *43*(12), 12287–12294. https://doi.org/10.1002/2016GL071676

Matthias, V., & Ern, M. (2018). On the origin of the mesospheric quasi-stationary planetary waves in the unusual arctic winter 2015/2016. *Atmospheric Chemistry and Physics*, *18*(7), 4803–4815. https://doi.org/10.5194/acp-18-4803-2018

Miller, S. D., Mills, S., Elvidge, C., Lindsey, D., Lee, T., & Hawkins, J. (2012). Suomi satellite brings to light a unique Frontier of nighttime environmental sensing capabilities. *Proceedings of the National Academy of Sciences of the United States of America*, *109*(39), 15706–15711. https://doi.org/10.1073/pnas.1207034109

Miller, S. D., Straka, W., III., Mills, S. P., Elvidge, C. D., Lee, T. F., Solbrig, J., et al. (2013). Illuminating the capabilities of the suomi national polar-orbiting partnership (NPP) visible infrared imaging radiometer suite (VIIRS) day/night band. *Remote Sensing*, *5*(12), 6717–6766. https://doi.org/10.3390/rs5126717

Miller, S. D., Straka, W., Yue, J., Smith, S., Alexander, M., Hoffmann, L., et al. (2015). Upper atmospheric gravity wave details revealed in nightglow satellite imagery. *Proceedings of the National Academy of Sciences of the United States of America*, *112*(49), E6728–E6735. https://doi.org/10.1073/pnas.1508084112

Miller, S. D., Straka, W. I., Yue, J., Seaman, C., Xu, S., Elvidge, C., et al. (2018). The dark side of Hurricane Matthew-Unique perspectives from the day/night band. *Bulletin of the American Meteorological Society*, *99*(12), 2561–2574. https://doi.org/10.1175/bams-d-17-0097.1

Mixa, T., Dörnbrack, A., & Rapp, M. (2021). Nonlinear simulations of gravity wave tunneling and breaking over Auckland Island. *Journal of the Atmospheric Sciences*, *78*(5), 1567–1582. https://doi.org/10.1175/JAS-D-20-0230.1

O'Sullivan, D., & Dunkerton, T. J. (1995). Generation of inertia-gravity waves in a simulated life-cycle of baroclinic instability. *Journal of the Atmospheric Sciences*, *52*(21), 3695–3716. https://doi.org/10.1175/1520-0469(1995)052<3695:goiwia>2.0.co;2

Plougonven, R., Hertzog, A., & Teitelbaum, H. (2008). Observations and simulations of a large-amplitude mountain wave breaking over the Antarctic Peninsula. *Journal of Geophysical Research*, *113*(D16113). https://doi.org/10.1029/2007JD009739

Plougonven, R., & Zhang, F. (2014). Internal gravity waves from atmospheric jets and fronts. *Reviews of Geophysics*, *52*(1), 33–76. https://doi.org/10.1002/2012RG000419

Russell, J. M., III., Bailey, S. M., Gordley, L. L., Rusch, D. W., Horáni, M., Hervig, M. E., et al. (2009). The Aeronomy of Ice in the Mesosphere (AIM) mission: Overview and early science results. *Journal of Atmospheric and Solar-Terrestrial Physics*, *71*(3–4), 289–299. https://doi.org/10.1016/j.jastp.2008.08.011

Sato, K., Tanteno, S., Watanabe, S., & Kawatani, Y. (2012). Gravity wave characteristics in the southern hemisphere revealed by a high-resolution middle-atmosphere general circulation model. *Journal of the Atmospheric Sciences*, *69*(4), 1378–1396. https://doi.org/10.1175/JAS-D-11-0101.1

Sato, K., & Yoshiki, M. (2008). Gravity wave generation around the polar vortex in the stratosphere revealed by 3-hourly radiosonde observations at Syowa Station. *Journal of the Atmospheric Sciences*, *65*(12), 3719–3735. https://doi.org/10.1175/2008JAS2539.1

Senf, F., & Achatz, U. (2011). On the impact of middle-atmosphere thermal tides on the propagation and dissipation of gravity waves. *Journal of Geophysical Research*, *116*(D24). https://doi.org/10.1029/2011JD015794

Sheese, P. E., Llewellyn, E. J., Gattinger, R. L., & Strong, K. (2014). OH meinel band nightglow profiles from OSIRIS observations. *Journal of Geophysical Research: Atmospheres*, *119*(19), 11417–11428. https://doi.org/10.1002/2014JD021617

Shibuya, R., Sato, K., Tsutsumi, M., Sato, T., Tomikawa, Y., Nishimura, K., & Kohma, M. (2017). Quasi-12h inertia-gravity waves in the lower mesosphere observed by the PANSY radar at Syowa Station (39.6°E, 69.0°S). *Atmospheric Chemistry and Physics*, *17*(10), 6455–6476. https://doi.org/10.5194/acp-17-6455-2017

Sica, R., Izawa, M. R. M., Walker, K. A., Boone, C., Petelina, S. V., Argall, P. S., et al. (2008). Validation of the atmospheric chemistry experiment (ACE) version 2.2 temperature using ground-based and space-borne measurements. *Atmospheric Chemistry and Physics*, *8*(1), 35–62. https://doi.org/10.5194/acp-8-35-2008

Snively, J. B., & Pasko, V. P. (2003). Breaking of thunderstorm-generated gravity waves as a source of short-period ducted waves at mesopause altitudes. *Geophysical Research Letters*, *30*(24), 2254. https://doi.org/10.1029/2003GL018436

Stephan, C., & Alexander, M. J. (2015). Realistic simulations of atmospheric gravity waves over the continental U.S. using precipitation radar data. *Journal of Advances in Modeling Earth Systems*, *7*(2), 823–835. https://doi.org/10.1002/2014MS000396

Stober, G., Jacobi, C., Matthias, V., Hoffmann, P., & Gerding, M. (2012). Neutral air density variations during strong planetary wave activity in the mesopause region derived from meteor radar observations. *Journal of Atmospheric and Solar-Terrestrial Physics*, *74*, 55–63. https://doi.org/10.1016/j.jastp.2011.10.007

Stober, G., Matthias, V., Jacobi, C., Wilhelm, S., Höffner, J., & Chau, J. L. (2017). Exceptionally strong summer-like zonal wind reversal in the upper mesosphere during winter 2015/16. *Annales Geophysicae*, *35*(3), 711–720. https://doi.org/10.5194/angeo-35-711-2017

Taylor, M. J., & Hapgood, M. A. (1988). Identification of a thunderstorm as a source of short period gravity waves in the upper atmospheric nightglow emissions. *Planetary and Space Science*, *36*(10), 975–985. https://doi.org/10.1016/0032-0633(88)90035-9

Triplett, C. C., Harding, B. J., Wu, Y.-J. J., England, S., Englert, C. R., Makela, J. J., et al. (2023). Large-scale gravity waves in daytime ICON-MIGHTI data from 2020. *Space Science Reviews*, *219*(1), 3. https://doi.org/10.1007/s11214-022-00944-w

Vadas, S. L. (2007). Horizontal and vertical propagation and dissipation of gravity waves in the thermosphere from lower atmospheric and thermospheric sources. *Journal of Geophysical Research*, *112*(A6), A06305. https://doi.org/10.1029/2006JA011845

Vadas, S. L., & Azeem, I. (2021). Concentric secondary gravity waves in the thermosphere and ionosphere over the continental United States on 25-26 March 2015 from deep convection. *Journal of Geophysical Research: Space Physics*, *126*(2), e2020JA028275. https://doi.org/10.1029/2020JA028275

Vadas, S. L., & Becker, E. (2018). Numerical modeling of the excitation, propagation, and dissipation of primary and secondary gravity waves during wintertime at McMurdo Station in the Antarctic. *Journal of Geophysical Research: Atmospheres*, *123*(17), 9326–9369. https://doi.org/10.1029/2017JD027974

Vadas, S. L., & Becker, E. (2019). Numerical modeling of the generation of tertiary gravity waves in the mesosphere and thermosphere during strong mountain wave events over the Southern Andes. *Journal of Geophysical Research: Space Physics*, *124*(9), 7687–7718. https://doi.org/10.1029/2019JA026694

Vadas, S. L., Becker, E., Bossert, K., Baumgarten, G., Hoffmann, L., & Harvey, V. L. (2023). Secondary gravity waves from the stratospheric polar vortex over ALOMAR Observatory on 12-14 January. *Journal of Geophysical Research: Atmospheres*, *128*(2), e2022JD036985. https://doi.org/10.1029/2022JD036985

Vadas, S. L., Becker, E., Figueiredo, C., Bossert, K., Harding, B., & Gasque, C. (2023). Primary and secondary gravity waves and global wind changes generated by the Tonga volcanic eruption on 15 January 2022: Modeling and comparison with ICON-MIGHTI winds. *Journal of Geophysical Research: Space Physics*, *128*(2), e2022JA031138. https://doi.org/10.1029/2022JA031138

Vadas, S. L., & Crowley, G. (2010). Sources of the traveling ionospheric disturbances observed by the ionospheric TIDDBIT sounder near Wallops Island on October 30, 2007. *Journal of Geophysical Research*, *115*(A7), A07324. https://doi.org/10.1029/2009JA015053

Vadas, S. L., Figueiredo, C., Becker, E., Huba, J. D., Themens, D. R., Hindley, N., et al. (2023). Traveling ionospheric disturbances induced by the secondary gravity waves from the Tonga eruption on 15 January 2022: Modeling with MESORAC-HIAMCM-SAMI3 and comparison with GPS/TEC and ionosonde data. *Journal of Geophysical Research: Space Physics*, *128*(6), e2023JA031408. https://doi.org/10.1029/2023JA031408

Vadas, S. L., & Fritts, D. C. (2001). Gravity wave radiation and mean responses to local body forces in the atmosphere. *Journal of the Atmospheric Sciences*, *58*(16), 2249–2279. https://doi.org/10.1175/1520-0469(2001)058<2249:gwramr>2.0.co;2

Vadas, S. L., Fritts, D. C., & Alexander, M. J. (2003). Mechanism for the generation of secondary waves in wave breaking regions. *Journal of the Atmospheric Sciences*, *60*(1), 194–214. https://doi.org/10.1029/2004JD005574

Vadas, S. L., & Liu, H.-L. (2009). Generation of large-scale gravity waves and neutral winds in the thermosphere from the dissipation of convectively generated gravity waves. *Journal of Geophysical Research*, *114*(A10), A10310. https://doi.org/10.1029/2009JA014108

Vadas, S. L., & Liu, H.-L. (2013). Numerical modeling of the large-scale neutral and plasma responses to the body forces created by the dissipation of gravity waves from 6 h of deep convection in Brazil. *Journal of Geophysical Research: Space Physics*, *118*(5), 2593–2617. https://doi.org/10.1002/jgra.50249

Vadas, S. L., Xu, S., Yue, J., Bossert, K., Becker, E., & Baumgarten, G. (2019). Characteristics of the quiet-time hotspot gravity waves observed by GOCE over the Southern Andes on 5 July 2010. *Journal of Geophysical Research: Space Physics*, *124*(8), 7034–7061. https://doi.org/10.1029/2019JA026693

Vadas, S. L., Yue, J., She, C.-Y., Stamus, P., & Liu, A. (2009). A model study of the effects of winds on concentric rings of gravity waves from a convective plume near Fort Collins on 11 May 2004. *Journal of Geophysical Research*, *114*(D6), D06103. https://doi.org/10.1029/2008JD010753

Vadas, S. L., Zhao, J., Chu, X., & Becker, E. (2018). The excitation of secondary gravity waves from local body forces: Theory and observation. *Journal of Geophysical Research: Atmospheres*, *123*(17), 9296–9325. https://doi.org/10.1029/2017JD027970

Walterscheid, R. L., Gelinas, L. J., Mechoso, C. R., & Schubert, G. (2016). Spectral distribution of gravity wave momentum fluxes over the Antarctic Peninsula from Concordiasi superpressure balloon data. *Journal of Geophysical Research: Atmospheres*, *121*(13), 7509–7527. https://doi.org/10.1002/2015JD024253

Walterscheid, R. L., Schubert, G., & Brinkman, D. G. (2001). Small-scale gravity waves in the upper mesosphere and lower thermosphere generated by deep tropical convection. *Journal of Geophysical Research*, *106*(D23), 31825–31832. https://doi.org/10.1029/2000jd000131

Watanabe, S., Sato, K., & Takahashi, M. (2006). A general circulation model study of the orographic gravity waves over Antarctica excited by katabatic winds. *Journal of Geophysical Research*, *111*(D18104). https://doi.org/10.1029/2005JD006851

Xu, S., Vadas, S., & Yue, J. (2024). Quiet time thermospheric gravity waves observed by GOCE and CHAMP. *Journal of Geophysical Research: Space Physics*, *129*(1). https://doi.org/10.1029/2023JA032078

Xu, S., Yue, J., Xue, X., Vadas, S., Miller, S. D., Azeem, I., et al. (2019). Dynamical coupling between Hurricane Matthew and the middle to upper atmosphere via gravity waves. *Journal of Geophysical Research: Space Physics*, *124*(5), 3589–3608. https://doi.org/10.1029/2018JA026453

Yoshiki, M., Kizu, N., & Sato, K. (2004). Energy enhancements of gravity waves in the Antarctic lower stratosphere associated with variations in the polar vortex and tropospheric disturbances. *Journal of Geophysical Research*, *109*, D23104. https://doi.org/10.1029/2004JD004870

Yoshiki, M., & Sato, K. (2000). A statistical study of gravity waves in the polar regions based on operational radiosonde data. *Journal of Geophysical Research*, *105*(17), 17995–18011. https://doi.org/10.1029/2000jd900204

Yue, J., Miller, S., Hoffmann, L., & Straka, W. C., III. (2014). Stratospheric and mesospheric concentric gravity waves over tropical cyclone Mahasen: Joint AIRS and VIIRS satellite observations. *Journal of Atmospheric and Solar-Terrestrial Physics*, *119*, 83–90. https://doi.org/10.1016/j.jastp.2014.07.003

Yue, J., Perwitasari, S., Xu, S., Hozumi, Y., Nakamura, T., Sakanoi, T., et al. (2019). Preliminary dual-satellite observations of atmospheric gravity waves in airglow. *Atmosphere*, *10*(11), 650. https://doi.org/10.3390/atmos10110650

Yue, J., Vadas, S. L., She, C.-Y., Nakamura, T., Reising, S. C., Liu, H.-L., et al. (2009). Concentric gravity waves in the mesosphere generated by deep convective plumes in the lower atmosphere near Fort Collins. *Journal of Geophysical Research*, *114*(D6), D06104. https://doi.org/10.1029/2008JD011244

Zhang, F. (2004). Generation of mesoscale gravity waves in upper-tropospheric jet-front systems. *Journal of the Atmospheric Sciences*, *61*(4), 440–457. https://doi.org/10.1175/1520-0469(2004)061<0440:gomgwi>2.0.co;2

Zülicke, C., & Peters, D. H. W. (2006). Simulation of inertia-gravity waves in a poleward breaking Rossby wave. *Journal of the Atmospheric Sciences*, *63*(12), 3253–3276. https://doi.org/10.1175/JAS3805.1